Geochemical Perspectives Letters

On the oxidation state of arc magmas

Y. Moussallam[1,2*], G. Georgeais[1], S. Ding[1,3], J.-L. Devidal[4], B. Scaillet[5], C. Oppenheimer[6], A. Burgisser[7], E.F. Rose-Koga[5], K.T. Koga[5], N. Peters[8], A. Peccia[1], P. Samaniego[4], N. Métrich[9], P. Robidoux[10,11,12], M. Kawaguchi[13]

OPEN ACCESS

https://doi.org/10.7185/geochemlet.2611

Abstract

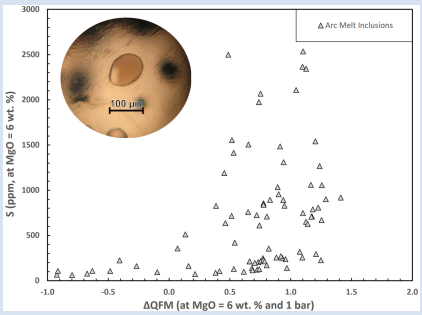

Arc magmas have long been considered significantly more oxidised than their ocean island and mid-ocean ridge counterparts, a characteristic widely attributed to infusion of the mantle wedge by fluids from subducted lithologies. However, here we show that at comparable degree of differentiation and sulfur content, arc magmas have comparable oxidation state to ocean island magmas. Our study is based on measurements of $Fe^{3+}/\Sigma Fe$ along with major and volatile elements in olivine and plagioclase hosted melt inclusions and matrix glasses from eleven volcanic systems located in arc settings worldwide. Accounting for fractional crystallisation (to MgO = 6 wt. %) we find that all systems lie on a reducing trend accompanying sulfur degassing, from QFM +0.9 (±0.2, 1σ) when S > 2000 ppm to QFM −0.2 (±0.6, 1σ) when S < 100 ppm (where QFM stands for the Quartz-Fayalite-Magnetite buffer). These findings reconcile the observed discrepancy between the oxidation states of xenoliths in arc magmas and gas emissions from arc volcanoes. We further show that fractional crystallisation influences the redox evolution of arc magmas to a comparable extent as, and sometimes counteracting, sulfur degassing.

Received 17 July 2025 | Accepted 5 March 2026 | Published 10 April 2026

Introduction

Constraining the oxidation state of arc magmas has long been of interest to petrologists and geochemists because the initial oxidation state of a melt plays a critical role in the sequence of phases that crystallise from it (*e.g.*, Osborn, 1959). Determining the oxidation state of the mantle source of these melts is in turn of interest for understanding the cycling of multiple valence state elements between the Earth's interior and exterior *via* subduction zones. Three main sample types have been used to constrain the oxidation state of arc magmas: (i) erupted lavas and tephra (*e.g.*, Carmichael, 1991), (ii) xenoliths carried in arc magmas (*e.g.*, Parkinson and Arculus, 1999), and (iii) crystal hosted melt inclusions (*e.g.*, Kelley and Cottrell, 2012).

However, while measurements of erupted products and xenoliths have been made for arc magmas around the world (*e.g.*, Hu *et al.*, 2024), measurements of crystal hosted melt inclusions (MIs) for arc lavas almost exclusively derive from a single site, the Mariana Arc (Brounce *et al.*, 2014; Kelley and Cottrell, 2009, 2012). One reason for the paucity of data of the latter type, in addition to challenging sample preparation, is that X-ray absorption near-edge structure (XANES) measurements of the valence state of Fe and S in water-rich silicate glasses are often compromised by beam damage (*e.g.*, Cottrell *et al.*, 2009, 2018; Shorttle *et al.*, 2015; Moussallam *et al.*, 2014, 2016, 2019, 2023). Yet these are the only measurements that directly measure the oxidation state of Fe and S (the most important multiple valence state elements) in the melt as opposed to reliance on proxies. Here we report $Fe^{3+}/\Sigma Fe$ measurements in melt inclusions from eleven arc volcanoes obtained by XANES spectroscopy at the iron K-edge, together with their volatile and major element concentrations.

1. Lamont-Doherty Earth Observatory, Columbia University, New York, USA
2. American Museum of Natural History, Department of Earth and Planetary Sciences, NY 10024, New York, USA
3. Department of Geological Sciences, University of Florida, Gainesville, FL, USA
4. Université Clermont Auvergne, CNRS, IRD, OPGC, Laboratoire Magmas et Volcans, F-63000 Clermont-Ferrand, France
5. ISTO, UMR 7327, Université d'Orléans-CNRS-BRGM, 1A rue de la Férollerie, 45071 Orléans cedex 2, France
6. Department of Geography, University of Cambridge, Downing Place, Cambridge, CB2 3EN, UK
7. Univ. Grenoble Alpes, Univ. Savoie Mont Blanc, CNRS, IRD, Univ. Gustave Eiffel, ISTerre, Grenoble, France
8. Department of Electronic and Electrical Engineering, University College London, UK
9. Université Paris Cité, Institut de Physique du Globe de Paris, CNRS, 75005 Paris, France
10. Universidad Andres Bello, Facultad de Ingenieria, Antonio Varas 880, Santiago, Chile
11. Millennium Institute on Volcanic Risk Research - Ckelar Volcanoes, Avenida Angamos 0610, Antofagasta, Chile
12. Consortium de Recherche en Exploration Minérale (CONSOREM), Département des Sciences Appliquées, Université du Québec à Chicoutimi, 555 Boul. de l'Université, Chicoutimi, Québec G7H 2B1, Canada
13. Earthquake Research Institute, University of Tokyo, Japan

* Corresponding author (email: yves.moussallam@ldeo.columbia.edu)

Samples and Methods

Sample sites were chosen because of the relatively mafic composition of their magmas (Fig. 1). They include Yasur, Aoba/Ambae, and Ambrym in Vanuatu, Shinmoedake and Aso in Japan, Okmok in Alaska, Fuego in Guatemala, San Cristóbal in Nicaragua, Cotopaxi in Ecuador, Villarrica in Chile, and Stromboli in Italy. Detailed sample description and processing is provided in the Supplementary Information, together with details of the Fourier Transform Infrared Spectroscopy and electron probe microanalyses.

XANES analyses. We performed Fe K-edge XANES spectroscopy at beamline I18 at the Diamond Light Source (DLS), UK. X-rays were focused with Kirkpatrick-Baez mirrors to a beam size of 5 μm (horizontal) × 5 μm (vertical). The beamline uses a liquid nitrogen cooled double crystal monochromator with silicon crystals and the Si (333) reflection was used to maximise the energy resolution. The measurements were performed in fluorescence mode. We used an energy dispersive Vortex ME-4 silicon drift detector positioned at 90° to the incident beam. The sample was positioned so that the normal to the sample surface was at 45° to the incident X-ray beam. Standard analytical conditions for XANES at I18 yield a photon flux of 10^{10} photon/s by attenuating (using a combination of aluminium foils and a slit) a 10^{12} photon/s primary beam upstream of the ion chamber. The beam can then be further attenuated (using Al foil).

We performed a series of tests to tune analytical conditions so as to avoid beam damage in our samples. We used:

1. A natural melt inclusion from Stromboli volcano (SHE750_cr1) containing 1.9 wt. % H_2O.
2. A natural melt inclusion from Okmok volcano (54D-MIol3) containing 2.0 wt. % H_2O.
3. A natural melt inclusion from Shinmoedake volcano (Shinm_cr23_mi) containing 2.2 wt. % H_2O.
4. A synthetic hydrated experimental glass of Villarrica 2015 composition (VillaS5_new_b) containing 4.5 wt. % H_2O.
5. A natural melt inclusion from Fuego volcano (F2018_cr12_mi) containing 6.2 wt. % H_2O.

We positioned the monochromator at a fixed energy of 7114 eV, corresponding to the oxidised peak of the pre-edge region. We then opened the shutter and counted the fluoresced X-rays every second for 660 to 1000 s (approx. 10 to 17 min) (Fig. 2). Tests were performed attenuating the beam with either 100 μm or 250 μm Al plates, resulting in attenuation to about 16 % and 1 % of the original flux respectively (equivalent to ~10^9 and ~10^8 photon/s respectively or ~10^8 and 10^7 photon/s/μm^2 respectively) (Moussallam *et al.*, 2019). We found that with 250 μm Al plates, henceforth referred to as the "high attenuation" setup, even a glass containing 6.2 wt. % H_2O could be analysed without beam damage under our analytical conditions. These conditions are similar to those of Moussallam *et al.* (2019) who showed that at the same beamline under the same analytical conditions no beam damage was occurring when analysing a glass with 5.2 wt. % H_2O. We found that with a 100 μm Al plate, conditions similar to those used by Moussallam *et al.* (2016, 2023), henceforth referred to as the "moderate attenuation" setup, glasses with up to 2.2 wt. % H_2O could be analysed without beam damage under our analytical conditions. All MIs containing more than 2.2 wt. % H_2O were therefore analysed using the high attenuation setup while the other melt inclusions, and all matrix glasses were analysed using the moderate attenuation setup. Because the high attenuation setup leads to fewer fluorescent photon counts and hence lower quality spectra, dwell time at each energy step was increased (energy step sizes and dwell times given in Table S-1) and three to four scans were acquired *per* melt inclusion and co-added. Spectra showing any structure in the edge and post-edge region were rejected (see Fig. S-6 in Moussallam *et al.*, 2014, for an example of contaminated spectra).

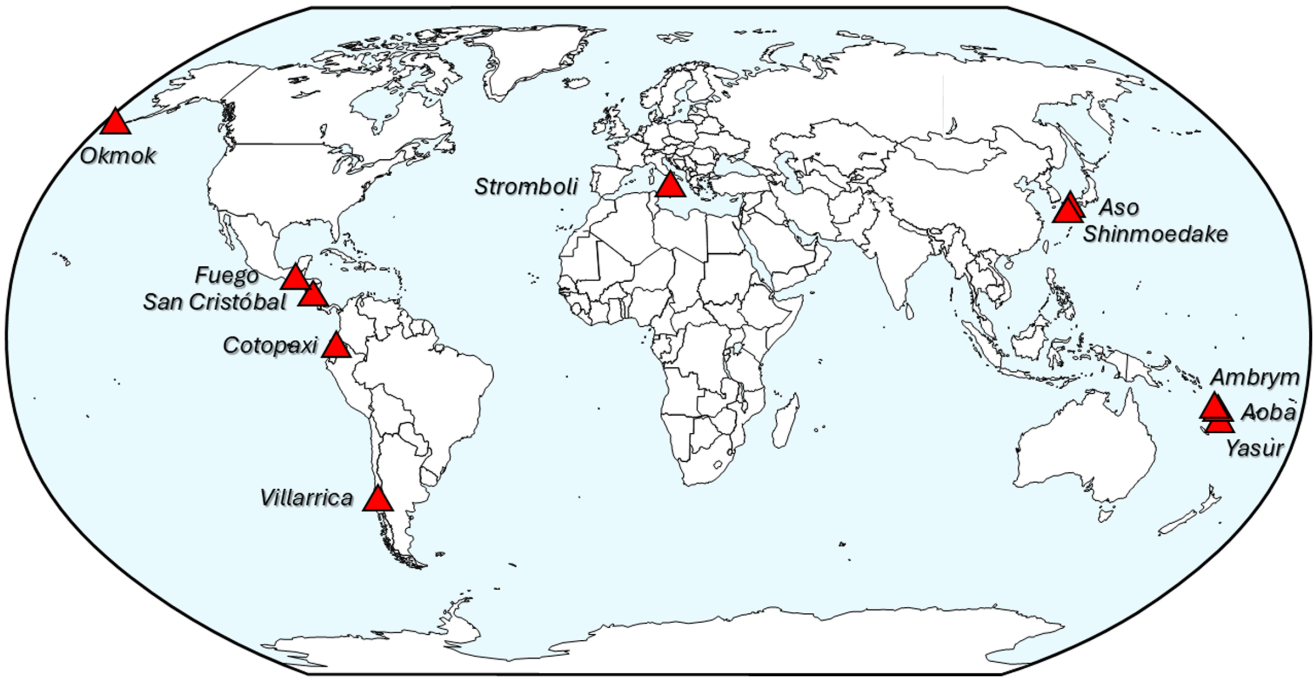

Figure 1 World map showing the locations of arc volcanoes investigated in this study, namely Yasur, Aoba/Ambae, Ambrym, Shinmoedake, Aso, Fuego, San Cristóbal, Cotopaxi, Villarrica, Okmok and Stromboli.

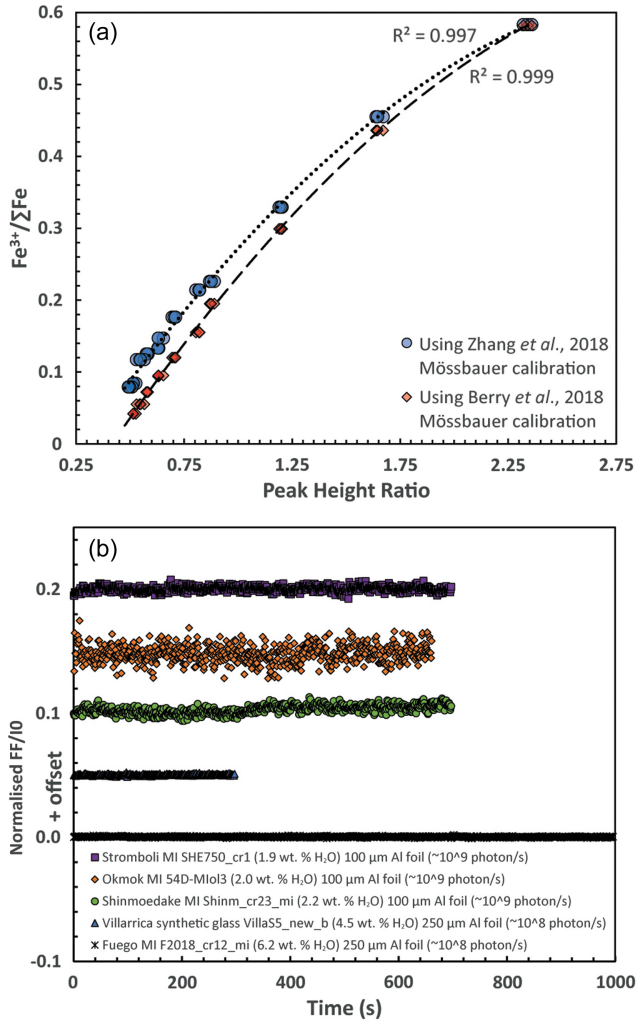

Figure 2 **(a)** Calibration line of the peak height ratio determined by XANES compared with $Fe^{3+}/\sum Fe$ ratios determined by Mössbauer spectroscopy in basaltic standard glasses from the Smithsonian NMNH (Mössbauer $Fe^{3+}/\sum Fe$ values from Zhang *et al.*, 2018 and Berry *et al.*, 2018 are shown). **(b)** Time series of normalised fluoresced intensity (FF) over I0 at 7114 eV integrated over 1 s intervals the five natural melt inclusions and synthetic glasses used for beam damage assessment. The Villarrica, Shinmoedake, Okmok and Stromboli glasses FF/I0 are offset by 0.05, 0.1, 0.15 and 0.2, respectively, for visibility. The variation in scatter between measurements is a function of the detector position which was adjusted between each sample.

The pre-edge region (7110–7118 eV) was fitted using a combination of a linear function and a damped harmonic oscillator function to fit the baseline and fitted by a combination of two gaussian functions. The relative intensity at the ~7112.2 eV and ~7114.0 eV peaks was then used to calibrate the spectra to the published $Fe^{3+}/\sum Fe$ ratios of the NMNH 117393 basalt reference glasses (Cottrell *et al.*, 2009) provided by the Smithsonian Institution National Museum of Natural History and using both the $Fe^{3+}/\sum Fe$ values reported in Zhang *et al.* (2018) and Berry *et al.* (2018) (Fig. 2). Repeat measurements ($n = 39$) on the twelve standards (all analysed using moderate attenuation) yielded a standard deviation of ±0.003 on the measured $Fe^{3+}/\sum Fe$ ratios (relative error) which translate to a standard deviation of ±0.04 on the calculated fO_2. Standard deviation using the high attenuation setup with two co-added spectra was determined as ±0.012 by Moussallam *et al.* (2019) (which translates to a standard deviation of ±0.14 on the calculated fO_2). We report this error here but note that in the present study we co-added three to four spectra each time so the error should be smaller. The absolute error is linked to the interpretation of the NMNH 117393 basalt reference glasses Mössbauer spectra and we show the calibrations resulting from both interpretations (Zhang *et al.*, 2018; Berry *et al.*, 2018) here.

Reverse fractional crystallisation calculation. To assess the effect of pre-entrapment crystallisation on $Fe^{3+}/\sum Fe$ (*e.g.*, Sun and Lee, 2022), we modelled reverse crystallisation paths for our melt inclusions using Petrolog3 (Danyushevsky and Plechov, 2011). We used the model of Ford *et al.* (1983) for olivine, the model of Ariskin *et al.* (1993) for plagioclase and the model of Ariskin *et al.* (1988) for clinopyroxene. This combination was used as it yielded reverse fractional crystallisation paths that most closely reproduced the trend in CaO *vs.* MgO observed in the natural melt inclusions and matrix glasses data (Fig. S-4). Note that these models assume a fully incompatible behaviour for Fe^{3+} in the olivine, clinopyroxene and plagioclase phases. Reverse fractional crystallisation calculations, which yield restored values of $Fe^{3+}/\sum Fe$, volatile contents, and major element compositions, were performed until the melt reached a value of 6 wt. % MgO, the highest value recorded in the data set (Fig. S-4). An alternative, empirical, modelling approach is presented in the SI. Post-entrapment crystallisation (PEC) for olivine hosted inclusions was calculated using Petrolog3 assuming a closed system for oxygen. The resulting PEC estimates range from −21 to +3 %, with an average of −2 % and standard deviation of ±3 %. Given these results we did not modify the MI compositions from their measured values.

Results and Discussion

We determined the $Fe^{3+}/\sum Fe$ ratio of 81 melt inclusions and 70 matrix glasses using XANES. The raw data for melt inclusions and matrix glasses are presented in Tables S-2 to S-6. We found that matrix glasses, clear of any visible alteration, exhibited a wide range of $Fe^{3+}/\sum Fe$ ratios, even within single samples. For instance, for Okmok glasses, $Fe^{3+}/\sum Fe$ ratios ranged from 0.19 to 0.54 (Tables S-5 and S-6). Most matrix glasses were significantly more oxidised than melt inclusions, with extreme values reaching up to QFM +5, uncorrelated with major or volatile element composition and with large variations in oxidation state recorded between areas of glass fragments located only a few millimetres apart. Based on these observations we consider that a significant proportion of our matrix glass $Fe^{3+}/\sum Fe$ measurements are unlikely to be representative of the original melt, and we consider that they reflect variable degrees of oxidation due to partial re-equilibration with erupted gas and/or the atmosphere during eruption. Consequently, we did not consider matrix glasses further in this study.

Raw melt inclusion $Fe^{3+}/\sum Fe$ ratios show no correlation with major or volatile (Fig. 3a) element compositions, with all r^2 values below 0.4. However, the analysed melt inclusions span a wide compositional range ($46.8 < SiO_2 < 62.8$ wt. %; Table S-3), partly reflecting variable degrees of differentiation. To account for this effect and compare melt inclusions at a common differentiation stage, we modelled reverse crystallisation paths using Petrolog3 (Danyushevsky and Plechov, 2011), back to MgO = 6 wt. % (results reported in Table S-7). After this restoration, a trend emerges between the oxidation state of melt inclusions and their S content (Fig. 3b,c). Melt inclusions with higher S contents are consistently more oxidised than those with lower S contents. On average, melt inclusions with S > 2000 ppm have an oxidation state of QFM +1.0 (±0.2, 1σ; $n = 6$), while those with S < 100 ppm have an oxidation state of QFM −0.2 (±0.6, 1σ; $n = 7$). Melt fO_2 is calculated from

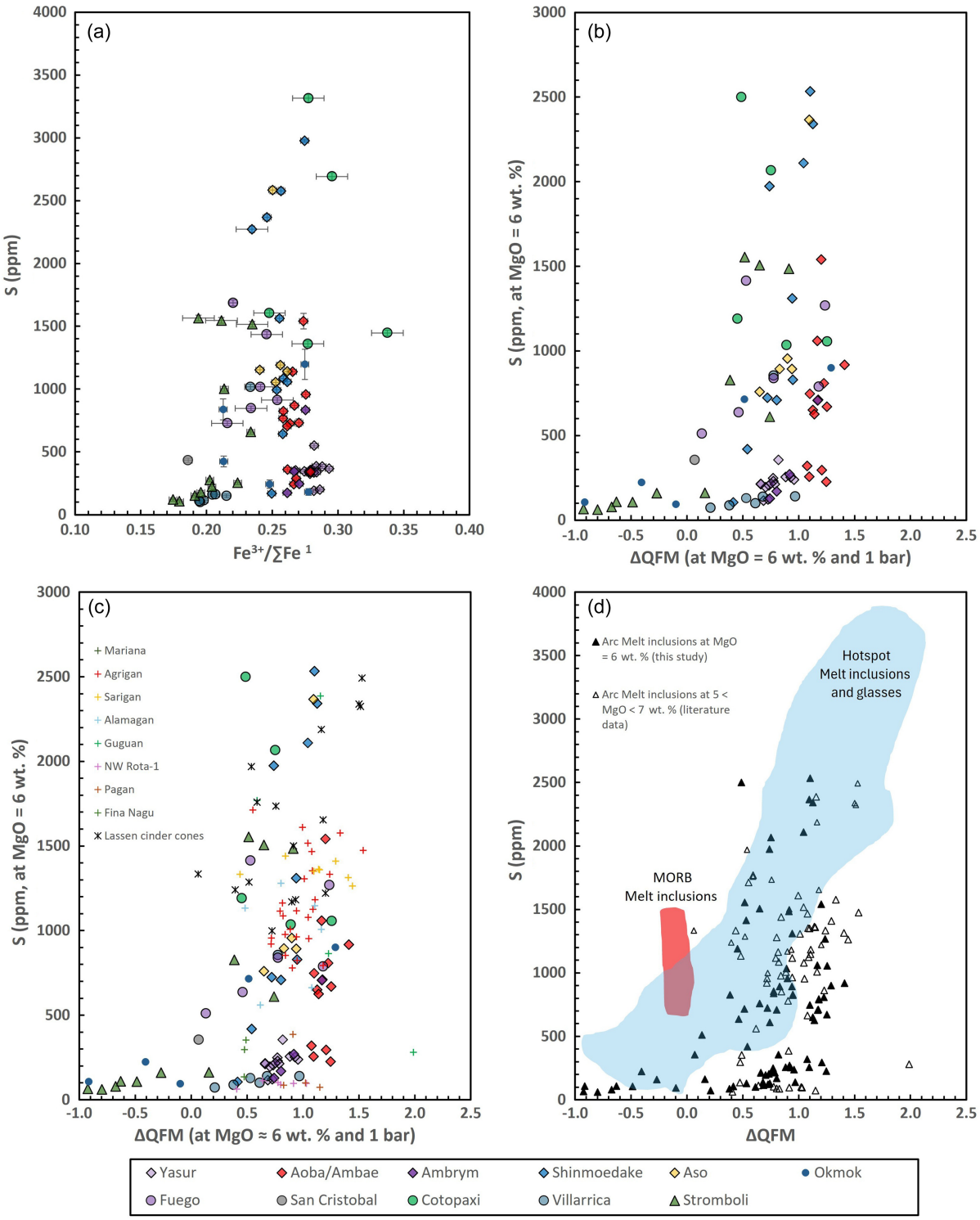

Figure 3 **(a)** Sulfur content *versus* oxidation state of melt inclusions plotted as $Fe^{3+}/\sum Fe$ calculated using the Mössbauer $Fe^{3+}/\sum Fe$ values from Zhang *et al.* (2018). Error bars show 1σ. **(b)** Sulfur content *versus* oxidation state (plotted as deviation from the QFM buffer using the equation of Kress and Carmichael, 1991) of melt inclusions after reversing fractional crystallisation to a common value of MgO = 6 wt. %. **(c)** Same as **(b)** with the addition of melt inclusions (and pillow glasses) data from the Marianna arc (Kelley and Cottrell, 2012; Brounce *et al.*, 2014, 2016) and Lassen cinder cones (Muth and Wallace, 2021), all with MgO contents between 5 and 7 wt. %. **(d)** Comparison between the sulfur content *versus* oxidation state fields recorded by melt inclusions, embayments and matrix glasses from arc volcanoes (same data set as in **(c)**), hotspot volcanoes (from Fig. 7 in Moussallam *et al.*, 2019) and mid-ocean ridge volcanoes (data set of Moussallam *et al.*, 2023) from the Southwest Indian Ridge). Note that Hotspot melt inclusions and glasses in the database used to draw the field are on average at MgO = 6.1 ± 1.0 wt. % while MORB Melt inclusions are on average at MgO = 6.4 ± 1.3 wt. % (1σ).

$Fe^{3+}/\sum Fe$ using Equation (7) from Kress and Carmichael (1991) at 1 bar and using the Petrolog3 calculated equilibrium temperature; QFM refers to the Quartz-Magnetite-Fayalite mineral redox buffer as reported in Frost (1991).

We can compare these results with other studies that have determined the oxidation state of melt inclusions (and pillow glasses) in arc magmas by XANES spectroscopy at the Fe K-edge. These include studies in the Mariana arc (Kelley and Cottrell, 2012; Brounce *et al.*, 2014, 2016) and a study of cinder cones in the Lassen region (California, USA) (Muth and Wallace, 2021). For the comparison with our data, corrected to MgO = 6 wt. %, to be meaningful, we only report in Figure 3c literature data from Mariannas and Lassen with MgO contents between 5 and 7 wt. % (*i.e.* directly comparable to our MgO = 6 wt. % data). The distributions of our new data points and existing ones coincide and overlap, mostly falling within the same range in oxidation state at a given S content. The observed trend between the sulfur content of melt inclusions and their oxidation state is strengthened by the addition of literature data extending the trend to slightly higher oxidation states. It therefore appears that, as previously demonstrated for hotspot volcanoes (Moussallam *et al.*, 2014, 2016, 2019; Brounce *et al.*, 2017), sulfur degassing in arc volcanoes is accompanied by a reduction of the melt oxidation state. In the SI we explore how available gas-melt equilibrium degassing models compare to the observed trend.

We note that our observations reconcile an apparent discrepancy in the literature regarding the oxidation states of arc magmas. Most estimates of the oxygen fugacities of the sub-arc mantle, from mineral oxybarometry in xenoliths and lavas (*e.g.*, Cottrell *et al.*, 2021 and references therein) or trace element systematics in arc lavas (*e.g.*, Zhao *et al.*, 2022) cluster around QFM +1, while those from the 'restoration' of volcanic gases of arc volcanoes to magmatic temperatures cluster around QFM (Moussallam *et al.*, 2024). The one log unit difference in oxidation state can be readily explained by degassing (Fig. 3).

Another interesting result is that, at similar degrees of differentiation (MgO ≈ 6 wt. %) and sulfur contents (~2500 ppm), arc magmas are not more oxidised than their hotspot counterparts. Hotspot magmas record oxidation states around QFM +1.2 under these conditions and even more oxidised conditions at higher sulfur contents, taken as evidence of recycled oxidised crustal material brought out of the deep earth by mantle plumes (Moussallam *et al.*, 2019) (Fig. 3d). In fact, there is a significant overlap between the arc and hotspot data sets (Fig. 3d). However, the reducing trend with sulfur degassing differs between hotspot and arc magmas, showing a constant slope for hotspot magmas and a hockey stick trend for arc magmas. This difference is likely due to the significant variation in water content between the two magma types. In contrast, the oxidation state of melt inclusions in mid-ocean ridge magmas shows no change in oxidation state with sulfur content (*e.g.*, Moussallam *et al.*, 2023) (Fig. 3d). The sulfur content of MORB is thought to be primarily controlled by equilibrium with sulfide (*e.g.*, Mathez, 1976), such that sulfur degassing in MORBs is an uncommon, yet documented, process (*e.g.*, Shorttle *et al.*, 2015).

Conclusions

We have analysed the oxidation states of arc magmas from eleven volcanic systems by measuring $Fe^{3+}/\sum Fe$ ratios along with major and volatile elements in olivine and plagioclase hosted melt inclusions. Once corrected for the effect of fractional crystallisation, we found that arc magmas define a trend of decreasing oxidation state with decreasing sulfur content. Thus, both degassing and differentiation can influence redox conditions of arc magmas to a comparable magnitude yet potentially in opposing directions (reducing and oxidising, respectively). When compared at similar degrees of differentiation and sulfur contents, the oxidation states of arc magmas can be similar to those of hotspot volcanoes.

Acknowledgements

Analytical work was carried out at Diamond Light Source using beamline I18 (proposal number SP36021-1) with invaluable support from Susan Nehzati and Konstantin Ignatyev. EFR-K thank Dr Akira Yoshiasa, and Dr. Toshiaki Hasenaka for their help on the field during the 2020 sampling campaign in Japan. We are very grateful to Marco Pistolesi for providing samples from Stromboli. We are grateful to Ery Hughes and two anonymous reviewers for providing valuable comments improving the quality of the manuscript.

Editor: Helen Williams

Open Research

Raw X-ray absorption near-edge structure spectra at the iron K-edge are archived on https://figshare.com/ [Moussallam, Y. (2025) ARC XANES SPECTRA RAW. *figshare*, dataset. https://doi.org/10.6084/m9.figshare.29509223.v1]. Raw FTIR data and PyIRoGlass outputs are archived on https://figshare.com/ [Moussallam, Y. (2025) ARC FTIR Spectra and Fit. *figshare*, dataset. https://doi.org/10.6084/m9.figshare.30657611.v1].

Additional Information

Supplementary Information accompanies this letter at https://www.geochemicalperspectivesletters.org/article2611.

Cite this letter as: Moussallam, Y., Georgeais, G., Ding, S., Devidal, J.-L., Scaillet, B., Oppenheimer, C., Burgisser, A., Rose-Koga, E.F., Koga, K.T., Peters, N., Peccia, A., Samaniego, P., Métrich, N., Robidoux, P., Kawaguchi, M. (2026) On the oxidation state of arc magmas. *Geochem. Persp. Let.* 39, 42–47. https://doi.org/10.7185/geochemlet.2611

References

Ariskin, A.A., Barmina, G.S., Frenkel, M.Y., Yaroshevskiy, A.A. (1988) Simulating low-pressure tholeiite-magma crystallization. *Geochemistry International* 25, 21–37.

Ariskin, A.A., Frenkel, M.Ya., Barmina, G.S., Nielsen, R.L. (1993) Comagmat: a Fortran program to model magma differentiation processes. *Computers & Geosciences* 19, 1155–1170. https://doi.org/10.1016/0098-3004(93)90020-6

Berry, A.J., Stewart, G.A., O'Neill, H.St.C., Mallmann, G., Mosselmans, J.F.W. (2018) A re-assessment of the oxidation state of iron in MORB glasses. *Earth and Planetary Science Letters* 483, 114–123. https://doi.org/10.1016/j.epsl.2017.11.032

Brounce, M.N., Kelley, K.A., Cottrell, E. (2014) Variations in $Fe^{3+}/\Sigma Fe$ of Mariana Arc Basalts and Mantle Wedge fO_2. *Journal of Petrology* 55, 2513–2536. https://doi.org/10.1093/petrology/egu065

Brounce, M., Kelley, K.A., Stern, R., Martinez, F., Cottrell, E. (2016) The Fina Nagu volcanic complex: Unusual submarine arc volcanism in the rapidly deforming southern Mariana margin. *Geochemistry, Geophysics, Geosystems* 17, 4078–4091. https://doi.org/10.1002/2016GC006457

Brounce, M., Stolper, E., Eiler, J. (2017) Redox variations in Mauna Kea lavas, the oxygen fugacity of the Hawaiian plume, and the role of volcanic gases in Earth's oxygenation. *Proceedings of the National Academy of Sciences* 114, 8997–9002. https://doi.org/10.1073/pnas.1619527114

Carmichael, I.S.E. (1991) The redox states of basic and silicic magmas: a reflection of their source regions? *Contributions to Mineralogy and Petrology* 106, 129–141. https://doi.org/10.1007/BF00306429

Cottrell, E., Kelley, K.A., Lanzirotti, A., Fischer, R.A. (2009) High-precision determination of iron oxidation state in silicate glasses using XANES. *Chemical Geology* 268, 167–179. https://doi.org/10.1016/j.chemgeo.2009.08.008

Cottrell, E., Lanzirotti, A., Mysen, B., Birner, S., Kelley, K.A., Botcharnikov, R., Davis, F.A., Newville, M. (2018) A Mössbauer-based XANES calibration for hydrous basalt glasses reveals radiation-induced oxidation of Fe. *American Mineralogist* 103, 489–501. https://doi.org/10.2138/am-2018-6268

Cottrell, E., Birner, S., Brounce, M., Davis, F., Waters, L., Kelley, K. (2021) Oxygen fugacity across tectonic settings. In: Moretti, R., Neuville, D.R. (Eds.) *Magma Redox Geochemistry*. American Geophysical Union, Hoboken, 33–61. https://doi.org/10.1002/9781119473206.ch3

Danyushevsky, L.V., Plechov, P. (2011) Petrolog3: Integrated software for modeling crystallization processes. *Geochemistry, Geophysics, Geosystems* 12, Q07021. https://doi.org/10.1029/2011GC003516

Ford, C.E., Russell, D.G., Craven, J.A., Fisk, M.R. (1983) Olivine-Liquid Equilibria: Temperature, Pressure and Composition Dependence of the Crystal/Liquid Cation Partition Coefficients for Mg, Fe^{2+}, Ca and Mn. *Journal of Petrology* 24, 256–266. https://doi.org/10.1093/petrology/24.3.256

Frost, B.R. (1991) Introduction to oxygen fugacity and its petrologic importance. *Reviews in Mineralogy and Geochemistry* 25, 1–9. https://doi.org/10.1515/9781501508684-004

Hu, F., Jiang, H., Wan, B., Ducea, M.N., Gao, L., Wu, F.-Y. (2024) Latitude-dependent oxygen fugacity in arc magmas. *Nature Communications* 15, 6050. https://doi.org/10.1038/s41467-024-50337-6

Kelley, K.A., Cottrell, E. (2009) Water and the Oxidation State of Subduction Zone Magmas. *Science* 325, 605–607. https://doi.org/10.1126/science.1174156

Kelley, K.A., Cottrell, E. (2012) The influence of magmatic differentiation on the oxidation state of Fe in a basaltic arc magma. *Earth and Planetary Science Letters* 329–330, 109–121. https://doi.org/10.1016/j.epsl.2012.02.010

Kress, V.C., Carmichael, I.S.E. (1991) The compressibility of silicate liquids containing Fe_2O_3 and the effect of composition, temperature, oxygen fugacity and pressure on their redox states. *Contributions to Mineralogy and Petrology* 108, 82–92. https://doi.org/10.1007/BF00307328

Mathez, E.A. (1976) Sulfur solubility and magmatic sulfides in submarine basalt glass. *Journal of Geophysical Research: Solid Earth and Planets* 81, 4269–4276. https://doi.org/10.1029/JB081i023p04269

Moussallam, Y., Oppenheimer, C., Scaillet, B., Gaillard, F., Kyle, P., Peters, N., Hartley, M., Berlo, K., Donovan, A. (2014) Tracking the changing oxidation state of Erebus magmas, from mantle to surface, driven by magma ascent and degassing. *Earth and Planetary Science Letters* 393, 200–209. https://doi.org/10.1016/j.epsl.2014.02.055

Moussallam, Y., Edmonds, M., Scaillet, B., Peters, N., Gennaro, E., Sides, I., Oppenheimer, C. (2016) The impact of degassing on the oxidation state of basaltic magmas: A case study of Kīlauea volcano. *Earth and Planetary Science Letters* 450, 317–325. https://doi.org/10.1016/j.epsl.2016.06.031

Moussallam, Y., Longpré, M.-A., McCammon, C., Gomez-Ulla, A., Rose-Koga, E.F., Scaillet, B., Peters, N., Gennaro, E., Paris, R., Oppenheimer, C. (2019) Mantle plumes are oxidised. *Earth and Planetary Science Letters* 527, 115798. https://doi.org/10.1016/j.epsl.2019.115798

Moussallam, Y., Georgeais, G., Rose-Koga, E.F., Koga, K.T., Hartley, M.E., Scaillet, B., Oppenheimer, C., Peters, N. (2023) CO_2-Undersaturated Melt Inclusions From the South West Indian Ridge Record Surprisingly Uniform Redox Conditions. *Geochemistry, Geophysics, Geosystems* 24, e2023GC011235. https://doi.org/10.1029/2023GC011235

Moussallam, Y., Oppenheimer, C., Scaillet, B. (2024) A novel approach to volcano surveillance using gas geochemistry. *Comptes Rendus. Géoscience* 356, 71–84. https://doi.org/10.5802/crgeos.158

Muth, M.J., Wallace, P.J. (2021) Slab-derived sulfate generates oxidized basaltic magmas in the southern Cascade arc (California, USA). *Geology* 49, 1177–1181. https://doi.org/10.1130/G48759.1

Osborn, E.F. (1959) Role of Oxygen Pressure in the Crystallization and Differentiation of Basaltic Magma. *American Journal of Science* 257, 609–647. https://doi.org/10.2475/ajs.257.9.609

Parkinson, I.J., Arculus, R.J. (1999) The redox state of subduction zones: insights from arc-peridotites. *Chemical Geology* 160, 409–423. https://doi.org/10.1016/S0009-2541(99)00110-2

Shorttle, O., Moussallam, Y., Hartley, M.E., Maclennan, J., Edmonds, M., Murton, B.J. (2015) Fe-XANES analyses of Reykjanes Ridge basalts: Implications for oceanic crust's role in the solid Earth oxygen cycle. *Earth and Planetary Science Letters* 427, 272–285. https://doi.org/10.1016/j.epsl.2015.07.017

Sun, C., Lee, C.-T.A. (2022) Redox evolution of crystallizing magmas with C-H-O-S volatiles and its implications for atmospheric oxygenation. *Geochimica et Cosmochimica Acta* 338, 302–321. https://doi.org/10.1016/j.gca.2022.09.044

Zhang, H.L., Cottrell, E., Solheid, P.A., Kelley, K.A., Hirschmann, M.M. (2018) Determination of $Fe^{3+}/\Sigma Fe$ of XANES basaltic glass standards by Mössbauer spectroscopy and its application to the oxidation state of iron in MORB. *Chemical Geology* 479, 166–175. https://doi.org/10.1016/j.chemgeo.2018.01.006

Zhao, S.-Y., Yang, A.Y., Langmuir, C.H., Zhao, T.-P. (2022) Oxidized primary arc magmas: Constraints from Cu/Zr systematics in global arc volcanics. *Science Advances* 8, eabk0718. https://doi.org/10.1126/sciadv.abk0718

Geochemical Perspectives Letters

On the oxidation state of arc magmas

Y. Moussallam, G. Georgeais, S. Ding, J.-L. Devidal, B. Scaillet, C. Oppenheimer, A. Burgisser, E.F. Rose-Koga, K.T. Koga, N. Peters, A. Peccia, P. Samaniego, N. Métrich, P. Robidoux, M. Kawaguchi

Supplementary Information

The Supplementary Information includes:

- Supplementary Text
- EPMA Standards
- Model Outputs
- Tables S-1 to S-7
- Figures S-1 to S-9
- Supplementary Information References

Supplementary Text

a) Detailed sample description and processing

The sample from Yasur (TAN 6), is a scoria lapilli described in Métrich *et al.* (2011) and attributed to a sub-Plinian eruption dated to 1400–800 yr BP (Nairn *et al.*, 1988). The phase assemblage consists of a few per cent of plagioclase, clinopyroxene and olivine phenocrysts and Fe-Ti oxide microlites in a highly vesicular glassy matrix (Métrich *et al.*, 2011). The sample from Aoba (also called Ambae) consists of lapilli from the 2017-2018 plinian eruption (Moussallam *et al.*, 2019). The phase assemblage consists of rare phenocrysts of plagioclase, olivine, and clinopyroxene, and microlites of the same phases and spinel in a glassy matrix (Moussallam *et al.*, 2019). The sample from Ambrym is described in Moussallam *et al.* (2021) and consists of lapilli from an intra-caldera, lava-fountain eruption. The phase assemblage includes olivine, plagioclase and clinopyroxene phenocrysts and glomerocrysts, sometimes associated with magnetite in a glassy vesicular matrix (Moussallam *et al.*, 2021). The sample from Shinmoedake is a lapilli-sized tephra for the 2011 eruption.

It comes from a mixed andesitic pumice from the Shinmoedake cone of the Kirishima volcanic group. The sampled layer corresponds to Unit 2 of (Miyabuchi *et al.*, 2013). The bulk composition is andesitic, containing phenocrysts of plagioclase, clinopyroxene, orthopyroxene, olivine, magnetite and ilmenite (Suzuki *et al.*, 2013). The Aso sample is a coarse black scoria fall deposit from the Kishimadake cone, that erupted 3.7 ka ago (Miyabuchi and Watanabe, 1997; Hirata *et al.*, 2020) and is further described in Kawaguchi *et al.* (2021). It is identified as the mafic end member of all Holocene Aso eruptions. The sample from Okmok is described in Peccia *et al.* (2023) and consists of scoria from ash fall and flow deposits from the 43 BCE Okmok II caldera-forming eruption. The phase assemblage includes plagioclase, clinopyroxene, orthopyroxene, titano-magnetite, and, in the flow deposit, rare olivine (Peccia *et al.*, 2023). The San Cristóbal sample (SC11D) was collected from the avalanche block layer located 600 m south of the San Cristóbal crater rim, belongs to a sequence of Holocene eruptions consisting of unconsolidated layers of homogeneous coarse scoriae and bombs of basaltic andesite composition covering a thick avalanche block layer (Robidoux *et al.*, 2017). The deposit was made of medium-to-coarse unconsolidated lapilli-sized scoriae. It contains ~50vol% phenocrysts of plagioclase, olivine, rare clinopyroxenes and highly vesiculated scoria from a XVIII century sub-plinian eruption (BA deposit: Havlicek *et al.*, 2000; Hazlett, 1977). The phase assemblage consists of phenocrysts of plagioclase, clinopyroxene, orthopyroxene and Fe-Ti oxides included into vesicular fragments. The sample from Fuego (VF18-AC4, provided by Terry Plank) is from the Fuego 2018 eruption and was collected from a rooftop 14.5 km away from the volcanic crater during the eruption (Shi *et al.*, 2021). It is a tephra fall deposit consisting of ash, lapilli and bombs with olivine, clinopyroxene and plagioclase in a trachy-andesity matrix (Taracsák *et al.*, 2023). The sample from Cotopaxi is described in Pistolesi *et al.* (2021) and originates from the upper part of the Layer 2, emitted during the 1744 eruption. The bulk composition is slightly more evolved than andesitic. Tephra matrix is mostly glassy with less than 5% microlites and 20% of phenocrysts, primarily plagioclase (90%), pyroxenes (8%), and olivine (<2%). The sample from Villarrica is described in Moussallam *et al.* (2023) and consists of agglutinate scoria, from the March 2015 lava fountain eruption. The phase assemblage consists of 68% matrix glass (highly vesiculated), 28% plagioclase, 2% olivine, 1%

clinopyroxene, and 0.2% chromian spinel (Moussallam *et al.*, 2023). Sample from Stromboli originate from several different eruptions major and paroxysmal. In chronological order, the 5 May 2003 paroxysmal eruption (ST345), the 24 of November 2009 major eruption, and both July and August 2019 paroxysmal eruptions (STG and SHE750, respectively). Each tephra shows mingling of two magma batches, a dark microlite-rich "high porphyric" (HP) black scoria from the shallower magma chamber and a light glassy "low porphyric" (LP) golden pumice from the deeper magma chamber. HP patches contain euhedral plagioclases, pyroxenes and olivines and LP patches are less crystalline and with smaller crystals but with more primitive olivines.

Crystal-hosted melt inclusions were found by lightly crushing, sieving, magnetically separating and hand-picking under a binocular microscope in the 0.5-2 mm size and 0.25-0.5 mm size fractions. Crystals were doubly polished using a corundum mat (to avoid carbon contamination) to expose the melt inclusion on two parallel sides. Melt inclusions from Yasur, Shinmoedake, Aso, Fuego, San Cristóbal, Cotopaxi, Villarrica and Stromboli were newly prepared for this study. Melt inclusions from Aoba/Ambae included both new preparations and existing samples from Moussallam *et al.* (2019). Melt inclusions from Ambrym were existing samples from Moussallam *et al.* (2021). Melt inclusions from Okmok were existing samples from Peccia *et al.* (2023). When using existing sets of melt inclusions, host crystals were removed from their existing mount and polished on the reverse side, parallel to the first polish, to obtain double-polished wafers, except for the Okmok samples where melt inclusions (large enough to be analysed by XANES without host contamination) were re-polished but only single-exposed. The newly polished side was the one used for XANES analyses. Melt inclusions were analysed first by FTIR, then by XANES and finally by EPMA. Photomicrographs of all MI are provided in Figure S-1.

b) Fourier Transform Infrared Spectroscopy (FTIR)

Volatile (H_2O, CO_2) contents in MIs and matrix glasses were determined using an N_2 purged Thermo Nicolet iN10mx FTIR at Lamont-Doherty Earth Observatory (LDEO). Depending on the sizes of the MIs and glasses, various aperture sizes (>25x25µm) were applied to maximize the FTIR signal without host crystal

contamination. For each measurement, 256 high resolution (2-4cm^{-1}) scans were applied from 400cm^{-1} to 8000cm^{-1} to include both near- and mid IR peaks for water. The background was measured prior to each transect and subsequently subtracted from each spectrum. Thickness of the doubly polished wafers were measured using a digital micrometer (Mitutoyo Digimatic Indicator). Baseline fitting and H_2O and CO_2 concentrations were determined using PyIRoGlass (https://github.com/sarahshi/PyIRoGlass; Shi *et al.*, 2024).

c) Electron probe microanalyses (EPMA)

The major element compositions of matrix glasses, MIs and their host crystals were measured with a Cameca SxFiveTactis electron microprobe at the Laboratoire Magmas et Volcans in Clermont-Ferrand during a single session (except for Okmok for which we report previous published EMPA from Peccia *et al.*, 2023). For crystalline phases (olivine and plagioclase), beam conditions of 15kV and 15 nA were employed (2µm beam size), with variable counting time ranging from 10 to 30s on peak as a function of element concentration to reduce detection limit (with off peak counting times similar to on peak ones). Errors in wt.% (one standard deviations based on 15 repeats on San Carlos olivine) are ± 0.19 for SiO_2, ± 0.01 for Al_2O_3, ± 0.09 for FeO, ± 0.04 for MnO, ± 0.01 for CaO, ± 0.12 for MgO, and ± 0.02 for NiO. For glass analyses, the beam current was decreased to 8 nA and the beam defocused to 10 µm. Sodium was analysed first to limit the effects of Na loss. Counting times of 10 s minimum were used (with off peak counting times similar to on peak ones). Error in wt.% (one standard deviations based on 23 repeats on standard glass VG-A99) are ± 0.18 for SiO_2, ± 0.05 for Na_2O, ± 0.04 for K_2O, ± 0.19 for Al_2O_3, ± 0.10 for CaO, ± 0.16 for FeO, ± 0.09 for MgO, ± 0.06 for TiO_2, ± 0.04 for MnO, and ± 0.04 for P_2O_5. The instrument was calibrated on natural and synthetic mineral standards and glasses: wollastonite (Si and Ca in glasses and plagioclase), San Carlos Olivine (Si in olivine), $MnTiO_3$ (Ti, Mn), orthoclase (K and Al in minerals), standard glass VG2 (Al in glasses), fayalite (Fe), forsterite (Mg), NiO (Ni), albite (Na) and apatite (P). Beam conditions for volatile measurements were 15kV, 40 nA and a 10µm defocused beam with a total counting time of 60s for Cl and 120s for S (sum of two spectrometers); S peak positions were carefully checked prior to analyses. Error (one standard deviations based on 10 repeats

on standard glasses Alvine and KE12) were 30 ppm and 48 ppm for S (alvine) and Cl (KE12) respectively. Standard repeat analyses are given in the accompanying supplementary EPMA standards spreadsheet (.xlsx), available for download from the online version of this article at https://doi.org/10.7185/geochemlet.2611.

d) Validity of the fractional crystallisation correction approach

While the calculated oxidation state of melt inclusions at MgO = 6 wt.% is model-dependent—and the use of Petrolog3, which assumes anhydrous conditions at 1 atm (conditions far removed from natural systems, especially for water-rich arc magmas), can be criticized—the emerging trend is robust and model-independent. This can be demonstrated using a fundamentally different approach.

We compiled all existing literature data for the Mariana arc (Kelley and Cottrell, 2012; Brounce *et al.*, 2014, 2016) and focused on melt inclusions with sulfur contents between 1350 and 1650 ppm. By narrowing the sulfur content range, we minimized the influence of sulfur degassing and targeted the least degassed portion of the dataset. Plotting sulfur content against oxidation state (Fig. S7A) reveals an empirical linear relationship ($R^2 = 0.6$), which we used to model the effects of fractional crystallization in our dataset.

The results of this empirical approach align closely with those of the original model (Fig. S7B). Using the empirical method, the same trend persists: melt inclusions with higher sulfur contents are consistently more oxidized than those with lower sulfur contents (Fig. S8). Quantitatively, melt inclusions with S > 2000 ppm exhibit an average oxidation state of QFM +1.0 (±0.2; 1σ), while those with S < 100 ppm average QFM +0.2 (±0.5; 1σ).

The agreement between two entirely independent modeling approaches—each with distinct assumptions and methodologies—lends strong confidence to the validity of our findings.

e) Sulfur degassing and oxidation state in arc magmas

Three gas–melt equilibrium, closed-system, degassing calculations were tested against the observed data trend. The first model is a modified version of the gas–melt equilibrium model by Gaillard and Scaillet (2009)

using the CO_2-H_2O solubility model of Iacono-Marziano *et al.* (2012). The second model is the D-Compress model by Burgisser *et al.* (2015). The third model is the Sulfur_X model by Ding *et al.* (2023).

In all three cases, two runs were performed. The first run was performed using the average composition of all MIs in our dataset at MgO = 6 wt.% (53.59±2.23 wt.% SiO_2; 0.89±0.29 wt.% TiO_2; 15.61±1.16 wt.% Al_2O_3; 9.12±1.77 wt.% FeO_t; 0.14±0.05 wt.% MnO; 6.00 wt.% MgO; 10.39±1.00 wt.% CaO; 2.70±0.36 wt.% Na_2O; 1.61±0.55 wt.% K_2O; 0.19±0.09 wt.% P_2O_5; errors given as 1 standard deviation) and the highest volatile contents measured in the dataset (2500 ppm S; 2000 ppm CO_2; 5 wt.% H_2O) as starting conditions (with no excess fluid). Temperature was set at 1150°C (as determined from Petrolog3 calculations), initial oxidation state was one log unit above the QFM buffer (calculated at 1 bar) corresponding to a $Fe^{3+}/\sum Fe$ of 0.24. We note that the absence of correlation between S and FeO content of the magmas points to no role of sulfide saturation in influencing the sulfur content of the melts (Fig. S-3). The second run was performed using the average composition of all MIs with 6 <MgO< 7 wt.% in the Muth and Wallace 2021 dataset of melt inclusion from scoria cones in the Lassen area (California, USA): 49.08±0.93 wt.% SiO_2; 1.07±0.22 wt.% TiO_2; 18.34±1.36 wt.% Al_2O_3; 7.92±1.52 wt.% FeO_t; 0.14±0.03 wt.% MnO; 5.83±0.47 wt.% MgO; 9.88±0.90 wt.% CaO; 3.53±0.28 wt.% Na_2O; 0.70±0.18 wt.% K_2O; 0.23±0.08 wt.% P_2O_5 and the highest volatile contents measured in that dataset: 2493 ppm S; 3.02 wt.% H_2O as starting conditions. As no CO_2 measurement is reported, the D-Compress run assumes 5757 ppm CO_2, and the Sulfur_X run assumes 5775 ppm CO_2. The starting pressure was set to 560 MPa, with no excess fluid, a temperature of 1150°C and the initial oxidation state was 1.5 log unit above the QFM buffer (calculated at 1 bar), as measured by Muth and Wallace (2021) for the most sulfur-rich and most oxidised melt inclusion in that dataset. All model outputs are reported in the additional supplementary model outputs spreadsheet (.xlsx), available for download from the online version of this article at https://doi.org/10.7185/geochemlet.2611.

In Run 1, all three models predict some degree of melt reduction associated with sulfur degassing (Fig. S-9). The Sulfur_X model aligns well with the most oxidized MIs in our dataset, particularly matching the trend defined by the Aoba/Ambae MIs. The D-Compress model corresponds well with some of the most

reduced MIs in our dataset but unfortunately concludes its calculations with predicted sulfur content remaining in the melt that are too high (600 ppm). The Gaillard and Scaillet (2009) model best reproduce the full magnitude of the observed change in oxidation state with sulfur content and matches best the trend defined by the Stromboli MIs. The observation that most of the change in oxidation state occurs during the last 500 ppm of sulfur degassing is well reproduced by the Gaillard and Scaillet (2009) and Sulfur_X models. Our modelling approach is intentionally limited to a first-order analysis, as additional magmatic processes, such as crustal assimilation and magma mixing, may have variably influenced oxidation states across different localities.

In Run 2 (Fig. S-9), the Gaillard and Scaillet (2009) model still predicts a reduction of the melt associated with sulfur degassing, reproducing, to a first order, the trend observed in the Lassen data and in the entire dataset. The D-Compress model also still predicts a reduction of the melt associated with sulfur degassing, with a trend aligned with the melt inclusions datasets but still concludes its calculations (at 1 bar) with a remaining sulfur content in the melt that is too high (790 ppm). The Sulfur_X model by contrast predicts that under these starting conditions sulfur degassing should be associated with oxidation of the melt, which is not consistent with the melt inclusions datasets.

Figure 3 in the main text shows that the oxidation state of arc magmas remains unchanged in the 2500 to 500 ppm S range, with most of the recorded change in oxidation state occurring between 500 and 0 ppm S. This is distinct from the trend observed in hotspot volcanoes (Fig. 3D). Two processes might, in part, explain this observation.

First, at greater pressure, H_2S is favored in the gas phase over SO_2, as a result S degassing from the melt can be redox-neutral as $S^{2-}_{(melt)}$ goes to $S^{2-}_{(gas)}$ (in the form of H_2S). At lower pressure however, SO_2 is strongly favored over H_2S in the gas phase, $S^{2-}_{(melt)}$ goes to $S^{4+}_{(gas)}$ (in the form of SO_2) liberating six electrons that can reduce Fe in the melt (Gaillard *et al.*, 2011). Degassing at shallower pressure (i.e., once less S remains in the melt) should hence be associated with a stronger reduction of the melt with S degassing.

It is worth noting that if sulfur was initially predominantly dissolved as S^{6+} in the melt, degassing as either SO_2 or H_2S in the gas phase would be expected to oxidize the remaining melt (by taking two and eight

electrons from the melt respectively, thus oxidizing Fe in the melt), a process which we do not observe in the current dataset.

The second process is the degassing of water. While most of the water dissolved in the melt will degas as H_2O in the gas phase — a redox-neutral reaction where $H_2O_{(Melt)}$ converts to $H_2O_{(gas)}$ — some of the water will produce H_2 in the gas phase via a reaction that could be written as $H_2O_{(Melt)} + 2FeO_{(Melt)} = H_{2(gas)} + Fe_2O_{3(melt)}$. Thus, the degassing of water should be associated with an oxidation of the melt (e.g., Candela, 1986; Burgisser and Scaillet, 2007; Humphreys *et al.*, 2015). In arc magmas, which are more water-rich than their hotspot counterparts, this effect is likely significant, counteracting to a large extent the reduction due to sulfur degassing.

Supplementary Tables

Table S-1 Acquisition parameters used during Fe K-edge XANES analysis.

Energy range (eV)	Step size (eV)	Dwell time (s)
For moderate attenuation (0.1 mm Al plate) Conditions:		
7020.0–7100.0	5	1
7101.0–7104.0	1	1
7104.1–7109.9	0.5	5
7110.0–7117.9	0.1	5
7118.0–7119.4	0.1	1
7119.5–7127.0	0.5	1
7128.0–7144.0	1	1
7148.0–7408.0	5	1
7410.0–7500.0	10	1
For high attenuation (0.25 mm Al plate) Conditions:		
7000.0–7100.0	10	2
7101.0–7104.0	1	2
7104.1–7109.9	0.5	15
7110.0–7117.9	0.1	15
7118.0–7119.4	0.1	3
7119.5–7127.0	0.5	2
7128.0–7144.0	1	2
7148.0–7408.0	5	2
7410.0–7500.0	10	2

Table S-2 Fe3+/∑Fe (1: calculated using Zhang *et al*., 2018 Mössbauer value and 2: calculated using Berry *et al*., 2018 Mössbauer value), ΔQFM (1: calculated using the Fe3+/∑Fe 1 ratio and the equation of Kress and Carmichael, 1991 and 2: calculated using the Fe3+/∑Fe 2 ratio and the equation of Kress and Carmichael, 1991) for all melt inclusions analysed together with volatile contents.

Table S-3 Major element compositions and melt inclusion and bubble dimensions. Error in wt.% on melt inclusions major elements (one standard deviations based on 23 repeats on A99 standard glass) are ± 0.18 for SiO2, ± 0.05 for Na2O, ± 0.04 for K2O, ± 0.19 for Al2O3, ± 0.10 for CaO, ± 0.16 for FeO, ± 0.09 for MgO, ± 0.06 for TiO2, ± 0.04 for MnO, and ± 0.04 for P2O5. Data for Okmok are from Peccia *et al.* (2023).

Table S-4 Mineral host major element compositions. Error in wt.% on host mineral phase major elements (one standard deviations based on 15 repeats on San Carlos olivine) are ± 0.19 for SiO2, ± 0.01 for Al2O3, ± 0.09 for FeO, ± 0.04 for MnO, ± 0.01 for CaO, ± 0.12 for MgO, and ± 0.02 for NiO. Data for Okmok are from Peccia *et al.* (2023).

Table S-5 Average, standard deviation, maximum and minimum values and number of analyses for Fe3+/∑Fe, ΔQFM, volatile contents and major element compositions of all glasses analysed at each volcano. [1] and [2] are as described in Table S-2 caption.

Table S-6 Fe3+/∑Fe (1: calculated using Zhang *et al.*, 2018 Mössbauer value and :2 calculated using Berry *et al.*, 2018 Mössbauer value), volatile contents and major element compositions of all glasses analysed at each volcano.

Table S-7 Fe3+/∑Fe, ΔQFM, volatile contents and major element compositions of Melt inclusions after reverse fractional crystallisation calculations to MgO=6 wt.%.

Tables S-2 to S-7 (.xlsx) are available for download from the online version of this article at https://doi.org/10.7185/geochemlet.2611.

Supplementary Figures

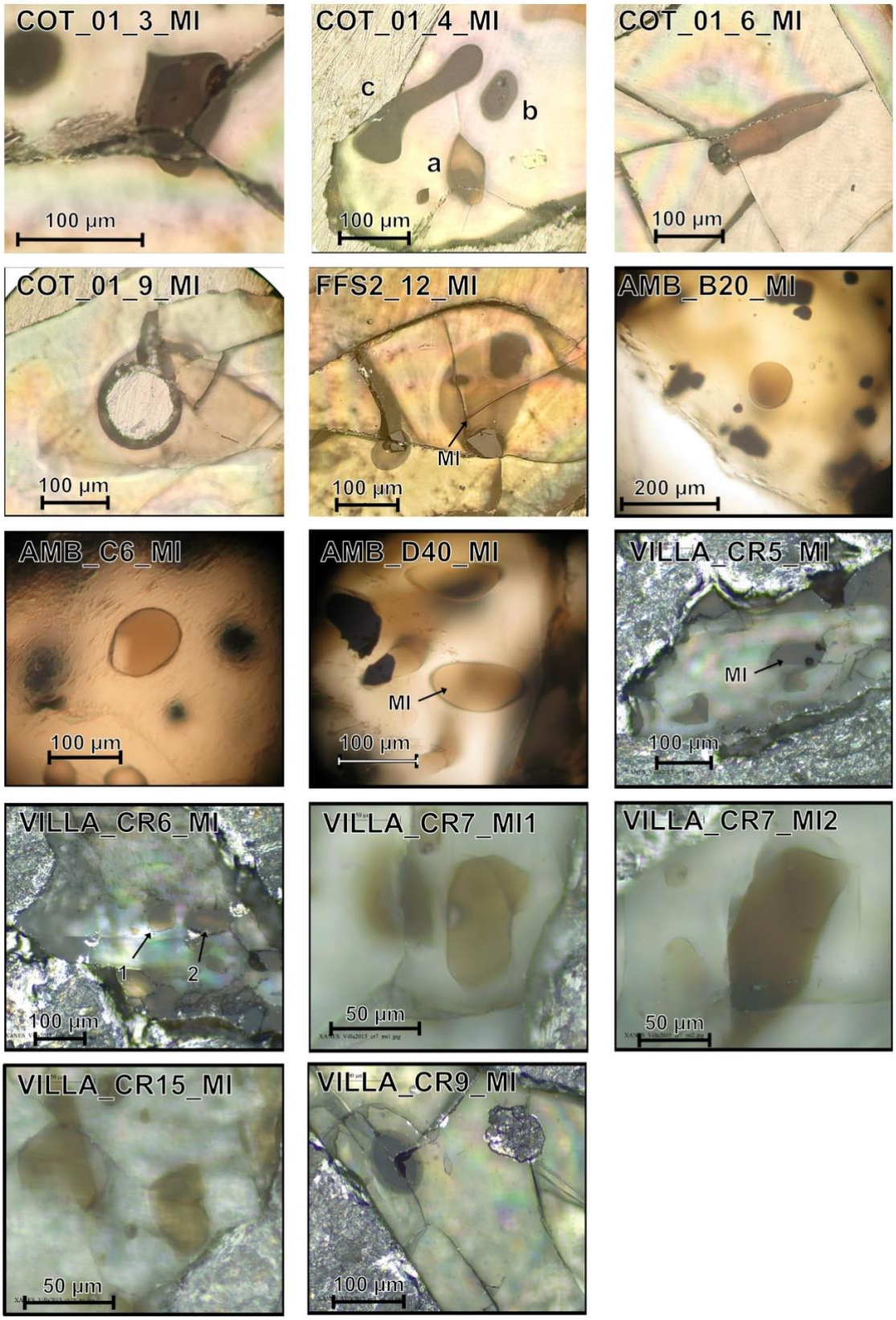

Figure S-1 Transmitted and reflected light microphotographs of all melt inclusions analysed.

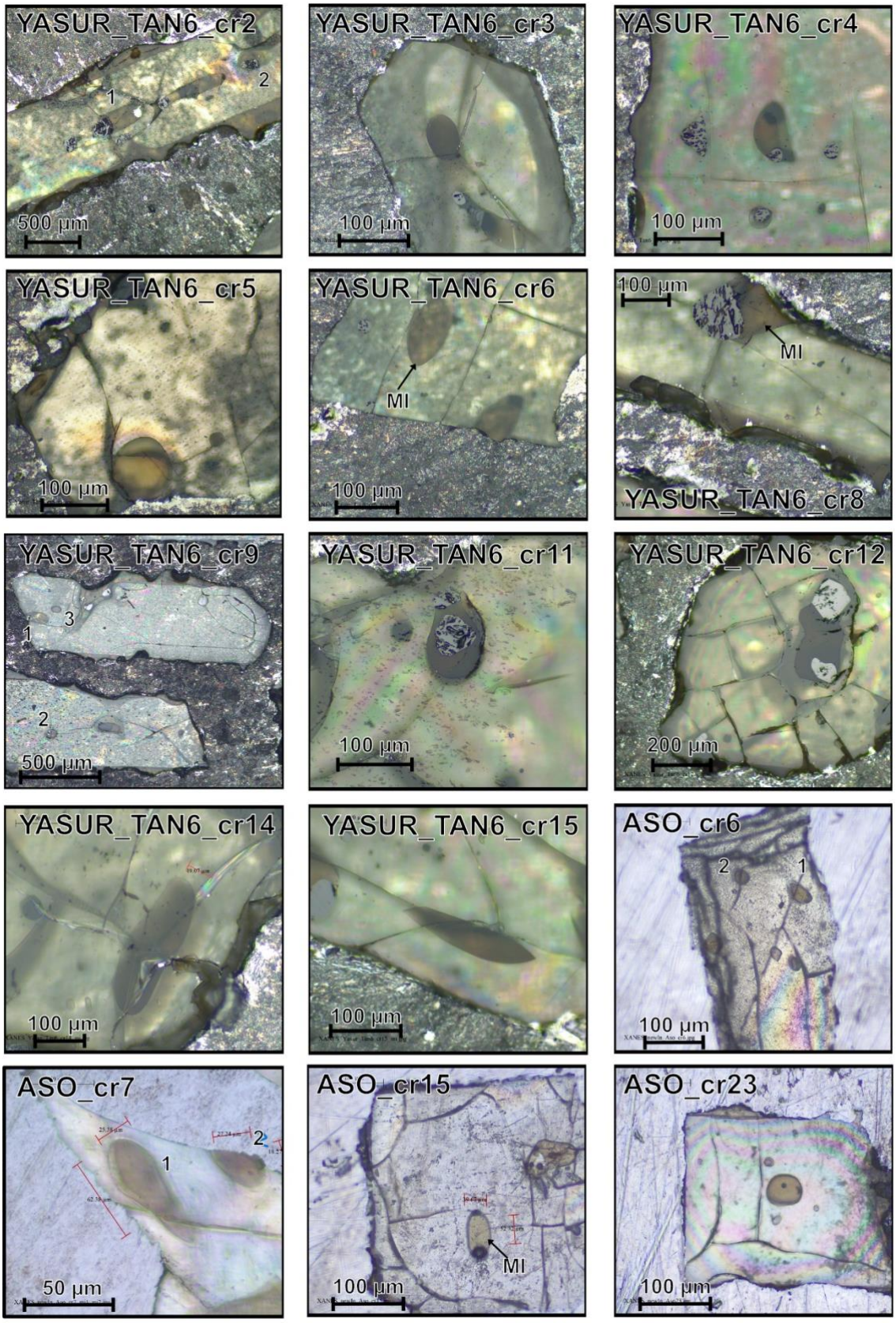

Figure S-1 continued.

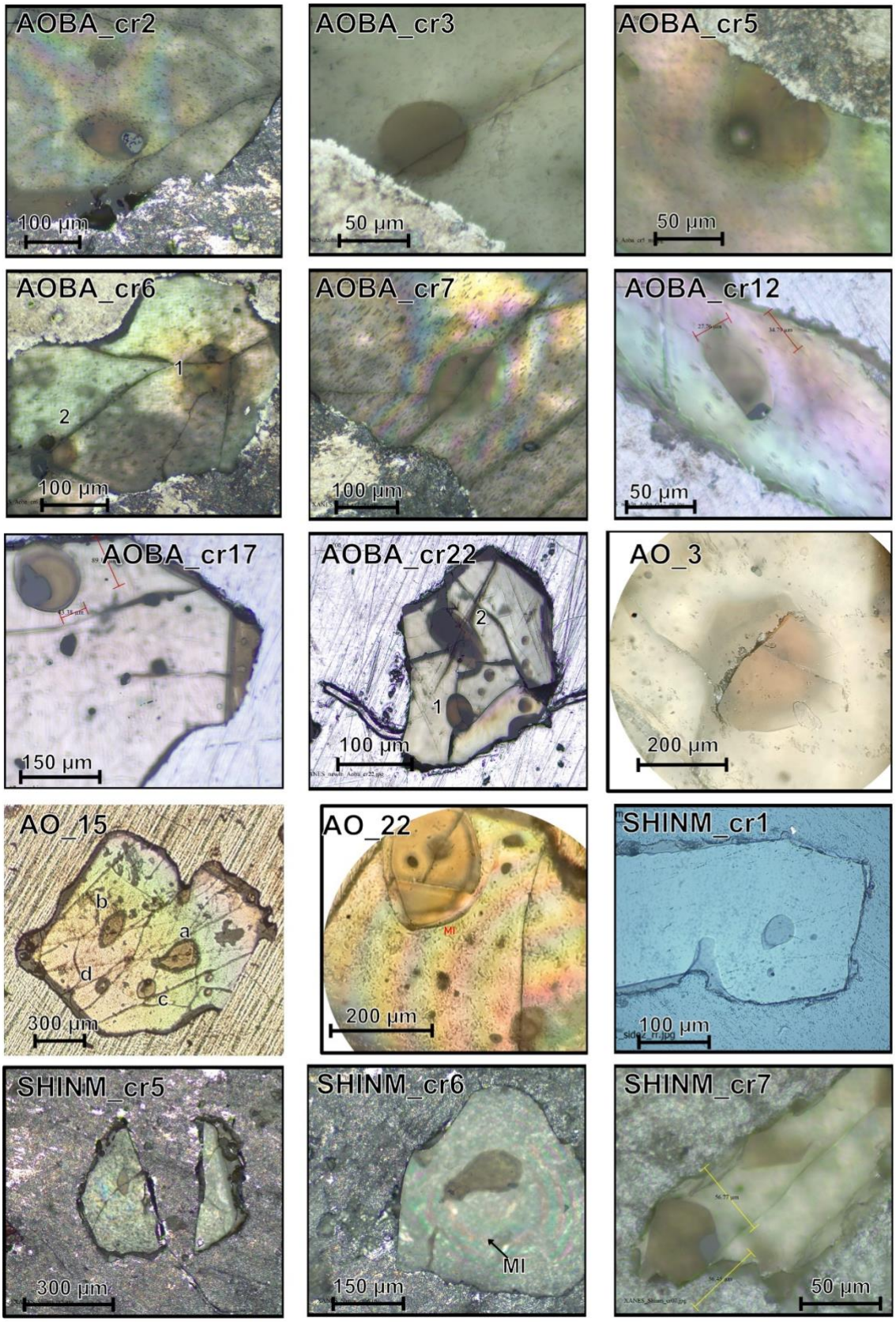

Figure S-1 continued.

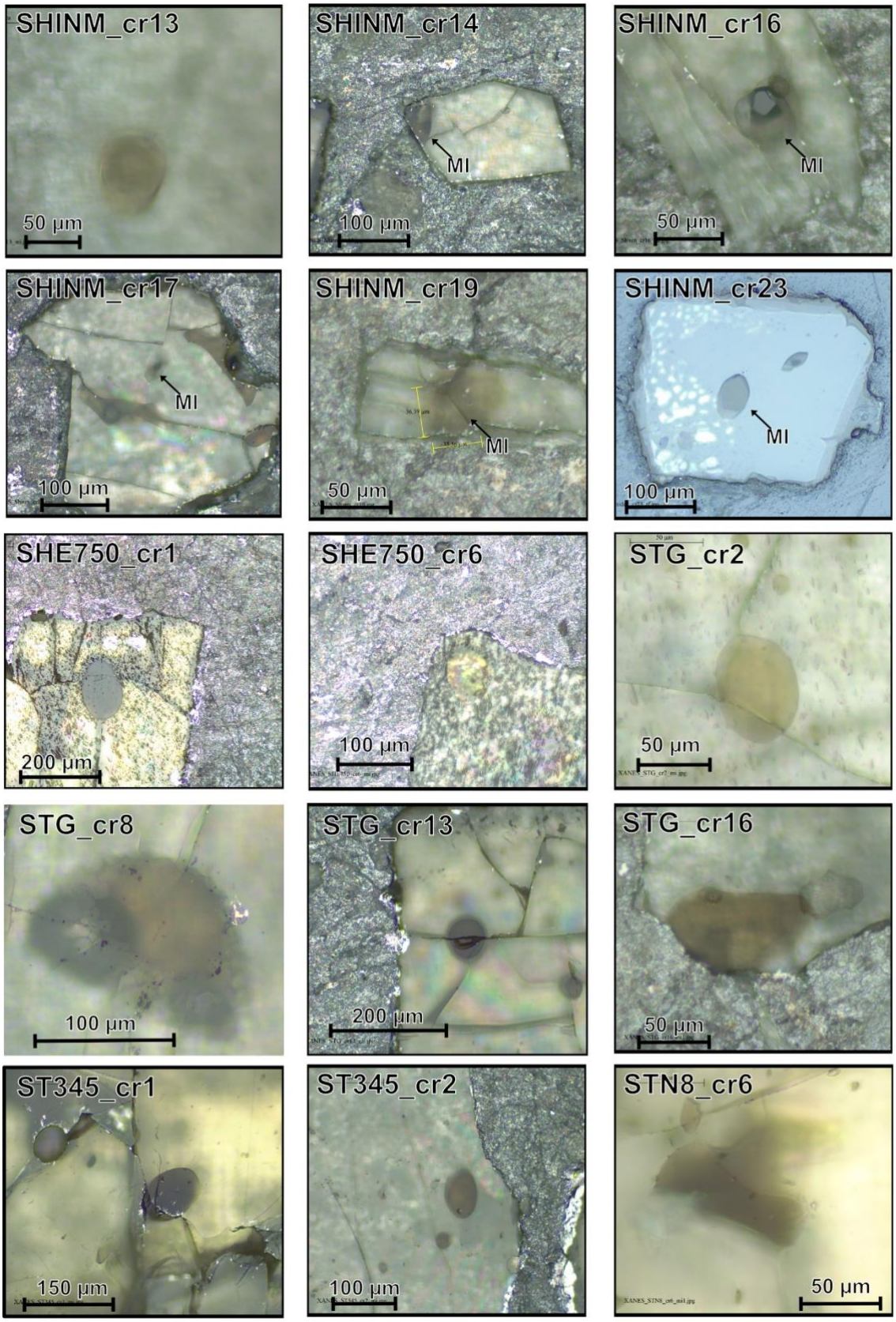

Figure S-1 continued.

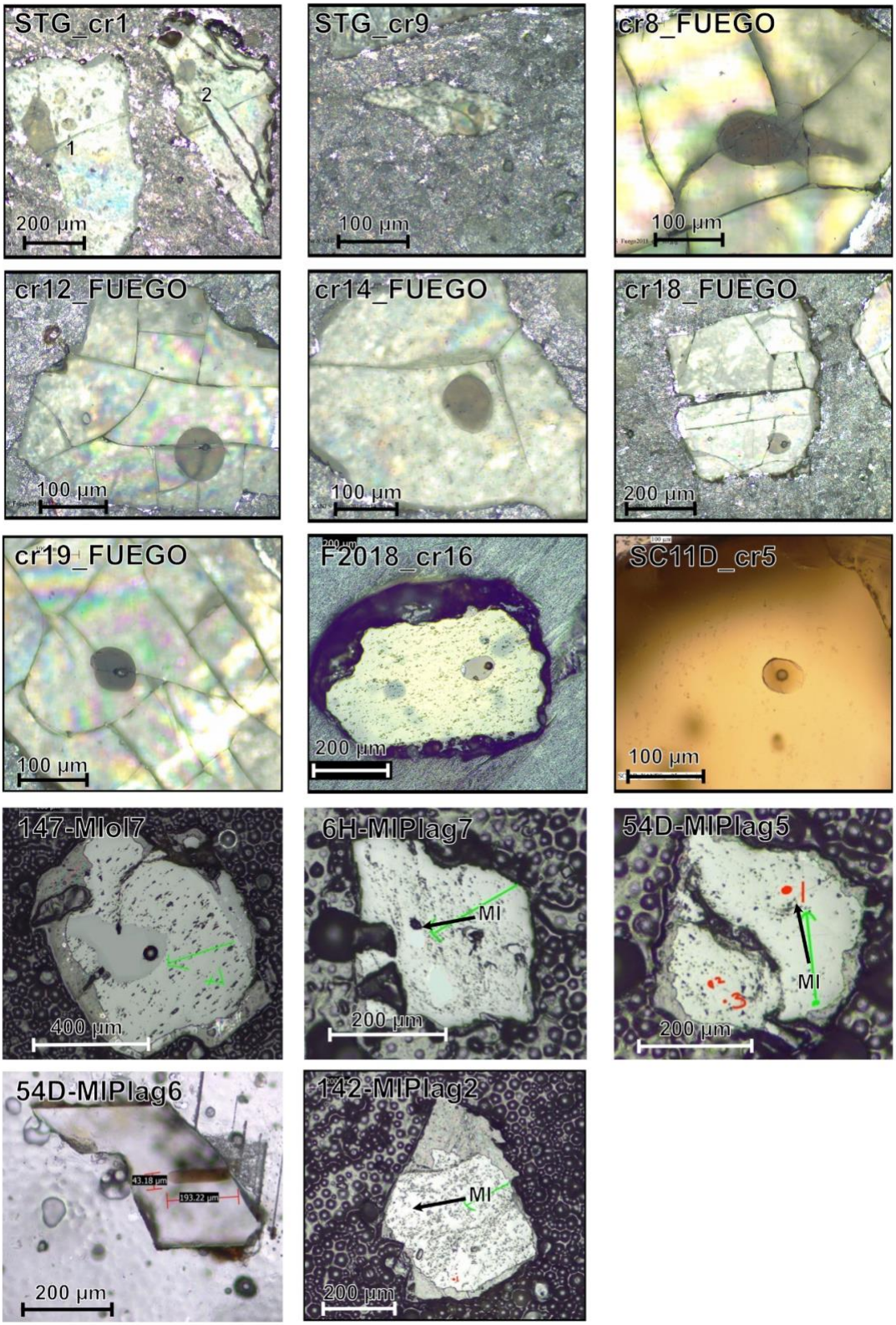

Figure S-1 continued.

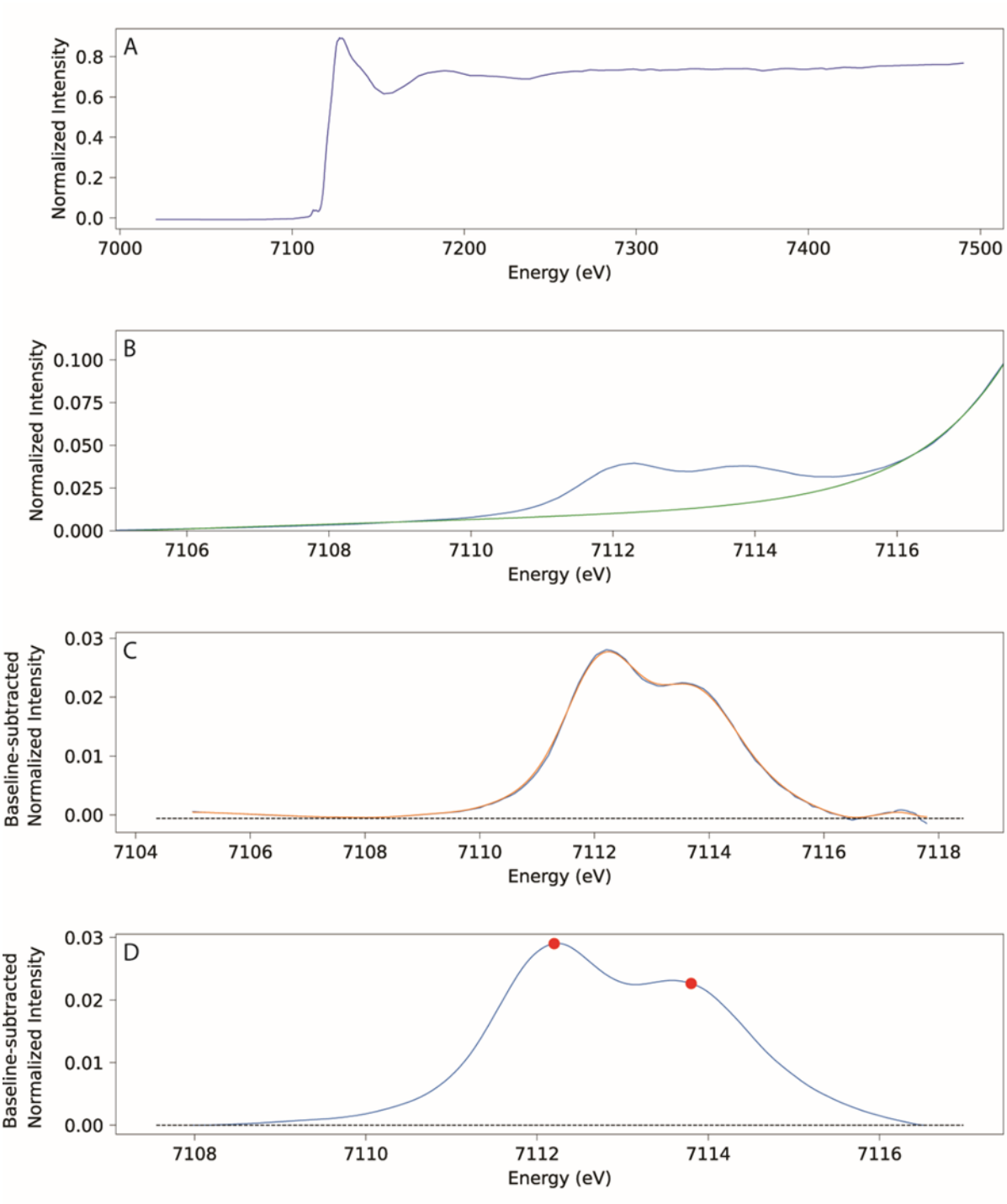

Figure S-2 Example of XANES spectra processing, on a spectrum obtained from a natural melt inclusion from Villarrica volcano. A. Edge-step normalized spectra. B. Pre-edge region fitting; green line shows the baseline absorption of the main Fe absorption edge (linear +DHO functions). **C**. Baseline-subtracted spectrum (blue), modelled as a combination of two gaussian functions (orange). D. Final pre-edge, the ratio of the baseline-subtracted normalized intensities at 7112.2 and 7113.8 eV (red dots) is extracted.

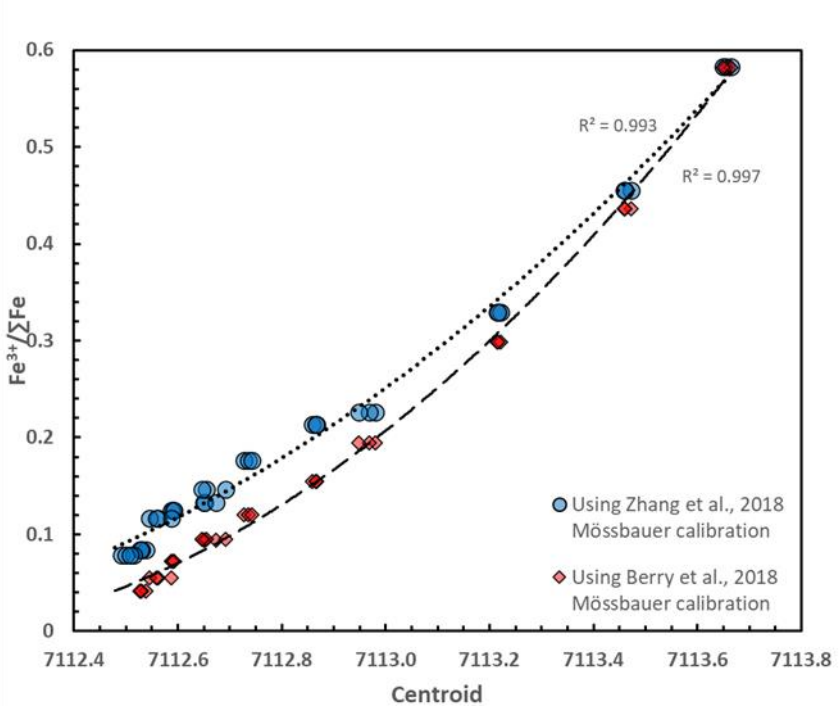

Figure S-3 Calibration lines based on the centroid energy position determined by XANES compared with $Fe^{3+}/\sum Fe$ ratios determined by Mössbauer spectroscopy in basaltic standard glasses from the Smithsonian NMNH (Mössbauer $Fe^{3+}/\sum Fe$ values from Zhang *et al.*, 2018 and Berry *et al.*, 2018 are shown). Note that the R^2 values on the 2nd degree polynomial fits are lower than when using the peak height ratio.

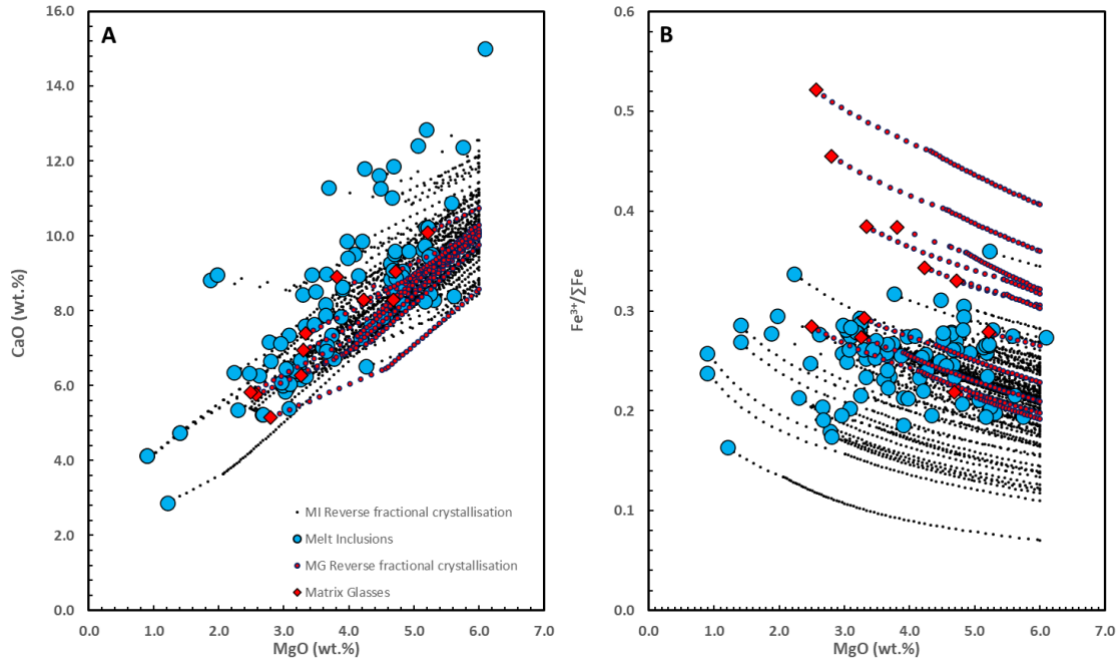

Figure S-4 The effect of pre-entrapment crystallization modelled on the composition (**A**) and oxidation state (**B**) of the melt inclusions and averages of matrix glasses. Reverse fractional crystallisation calculations were performed until the melt reaches a value of MgO=6wt.% using Petrolog3 (Danyushevsky and Plechov, 2011).

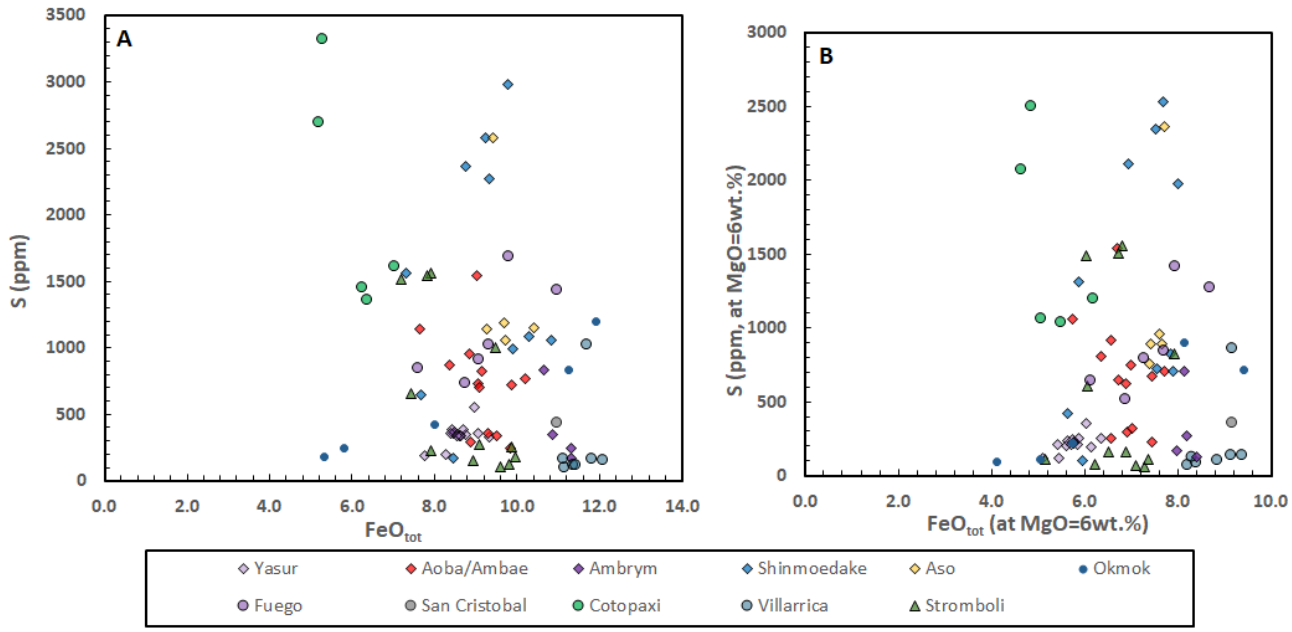

Figure S-5 Sulfur content versus FeO (total) in all melt inclusions. **A**. Raw data. **B**. Data after reverse fractional crystallization calculations to MgO=6wt.%.

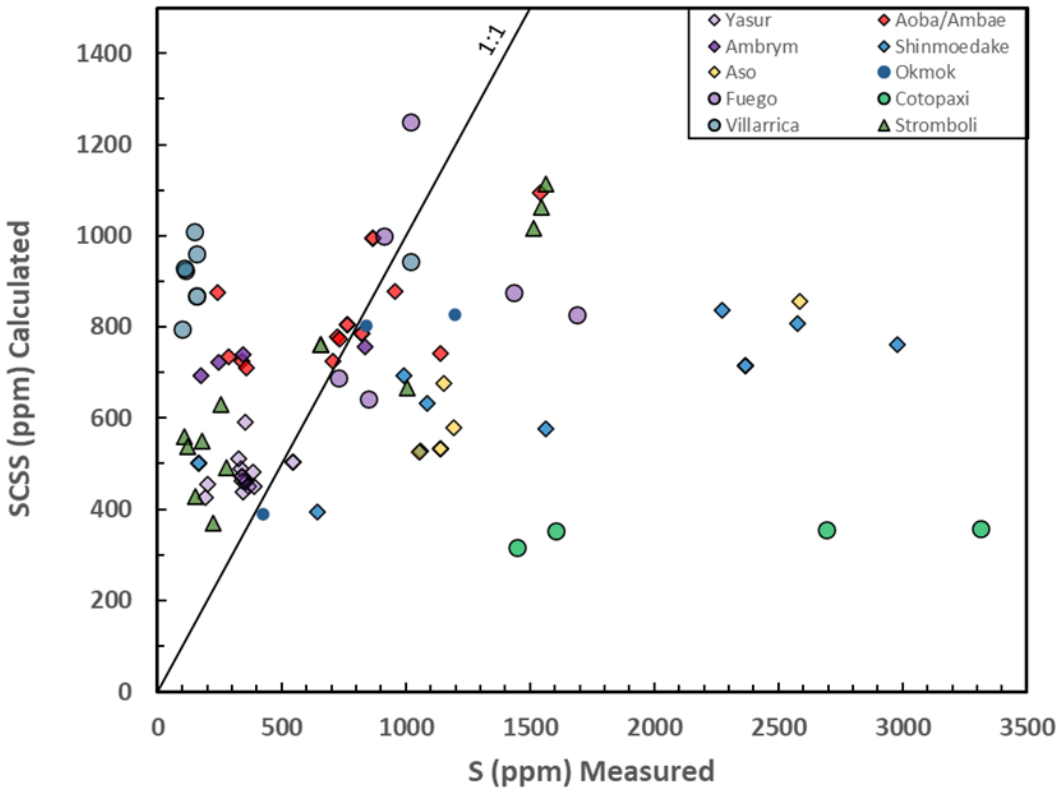

Figure S-6 Comparison between theoretical Sulfur content at sulfide saturation (calculated using the model of Fortin *et al.*, 2015) and measured sulfur content in melt inclusions. The absence of equivalence shows that the sulfur content of melt inclusions is not a reflection of equilibrium with sulfides.

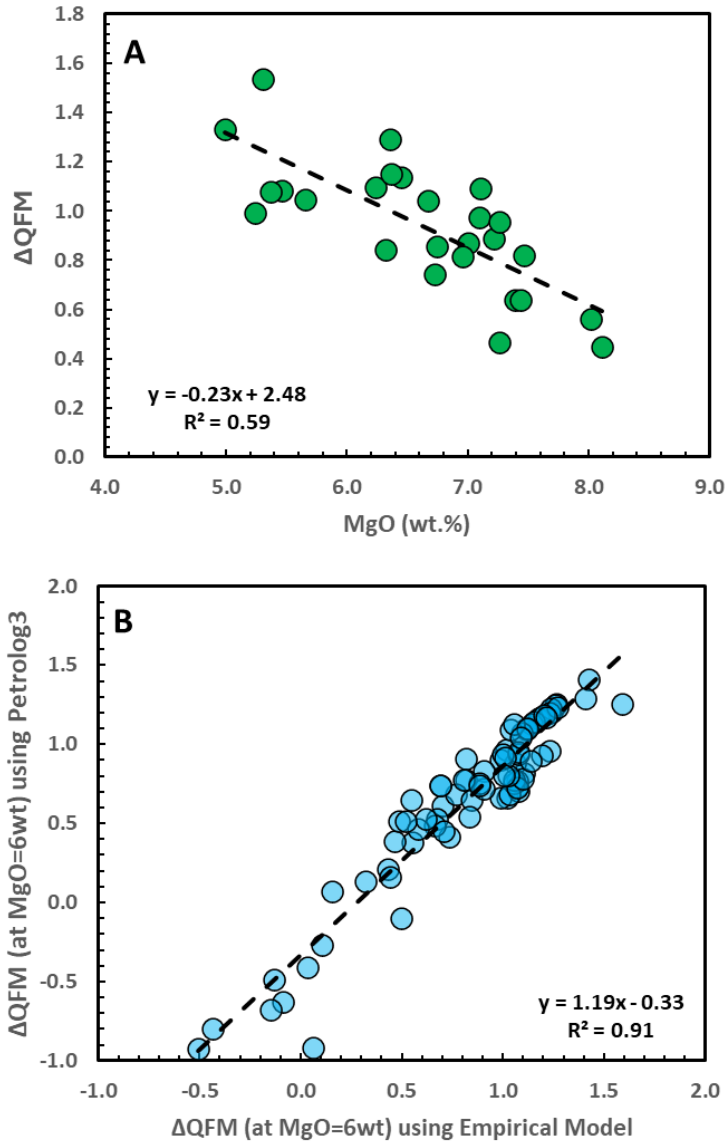

Figure S-7 **A**. Empirical relationship between MgO and oxidation state in melt inclusions and pillow glasses from the Mariannas over a narrow range in S content (1350 to 1650 ppm; original data from Kelley and Cottrell, 2012; Brounce *et al*., 2014, 2016, as reported in Cottrell *et al*., 2021). B. Comparison between oxidation state of melt inclusions (this study's dataset) after reversing fractional crystallization to a common value of MgO=6wt.% using either the empirical model approach or using Petrolog3.

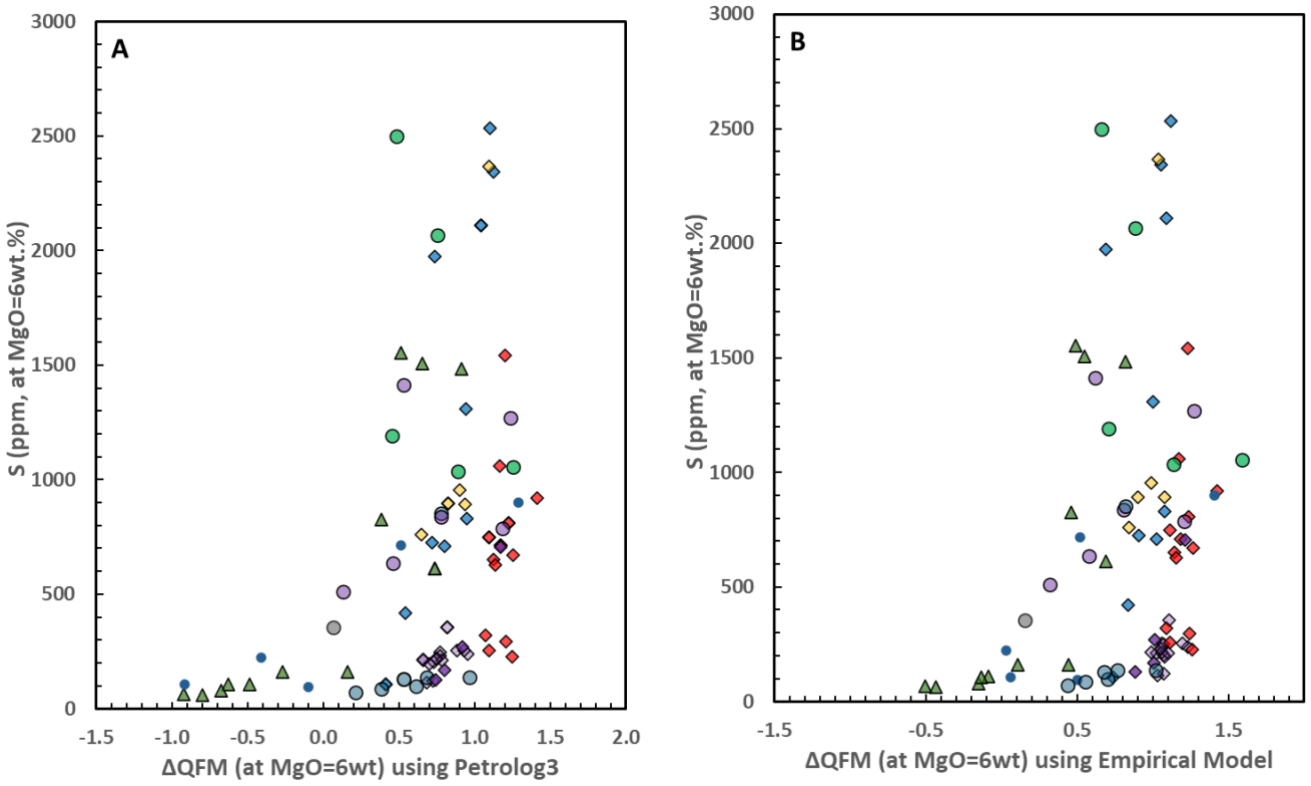

Figure S-8 Side by side comparison between the oxidation state of melt inclusions compared to their S content after reversing fractional crystallization to a common value of MgO=6wt.% using either Petrolog3 (**A**) or the empirical model approach (**B**). All symbols are the same as in Fig. 3 in the main text.

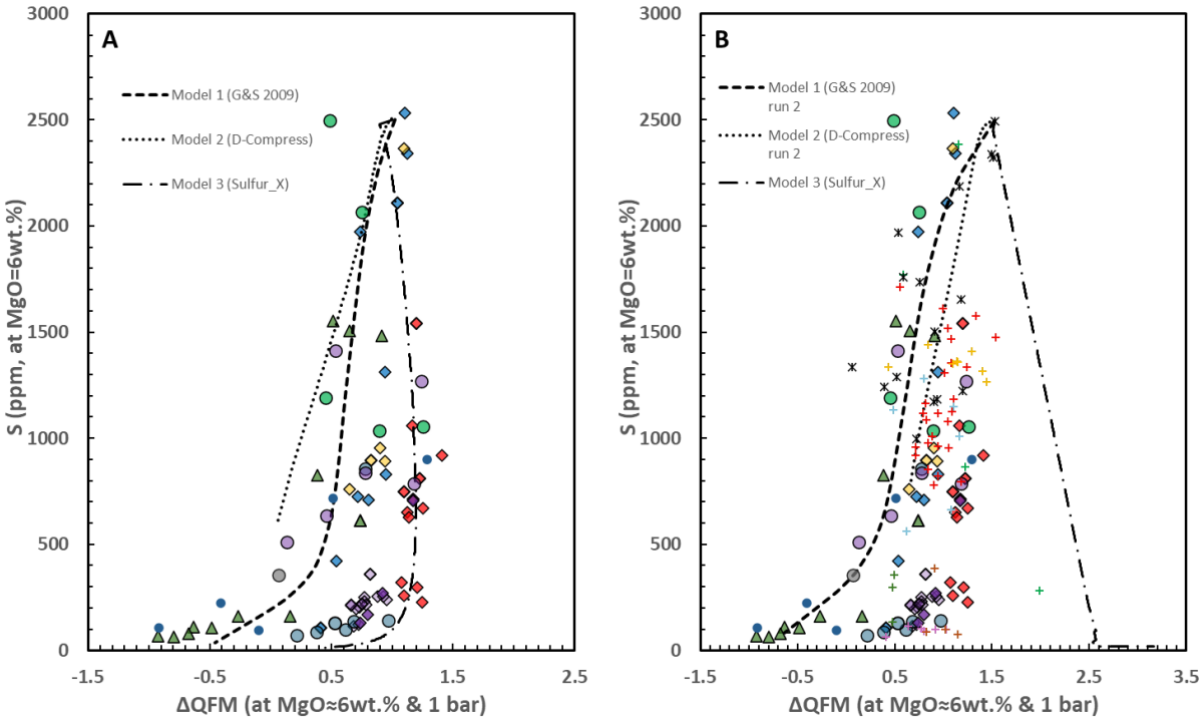

Figure S-9 **A.** Comparison between sulfur content and oxidation state of melt inclusions after reversing fractional crystallisation to a common value of MgO=6wt.% and the result of three forward modelling (closed-system, equilibrium) calculations of the effect of degassing for an average arc composition starting with 2500 ppm S; 2000 ppm CO_2; 5 wt.% H_2O and QFM+1. **B**. Same as A with the addition of melt inclusions (and pillow glasses) data from the literature, all with MgO content between 5 and 7 wt.%, and comparing with the result of three forward modelling (closed-system, equilibrium) calculations of the effect of degassing using the average composition of melt inclusions from Lassen cones, starting with 2500 ppm S; 3 wt.% H_2O at 560 MPa and QFM+1.5. All symbols are the same as in Fig. 3 in the main text.

Supplementary Information References

Berry, A.J., Stewart, G.A., O'Neill, H.St.C., Mallmann, G., Mosselmans, J.F.W. (2018) A re-assessment of the oxidation state of iron in MORB glasses. *Earth and Planetary Science Letters* 483, 114–123. https://doi.org/10.1016/j.epsl.2017.11.032

Brounce, M.N., Kelley, K.A., Cottrell, E. (2014) Variations in $Fe^{3+}/\sum Fe$ of Mariana Arc Basalts and Mantle Wedge fO_2. *Journal of Petrology* 55, 2513–2536. https://doi.org/10.1093/petrology/egu065

Brounce, M., Kelley, K.A., Stern, R., Martinez, F., Cottrell, E. (2016) The Fina Nagu volcanic complex: Unusual submarine arc volcanism in the rapidly deforming southern Mariana margin. *Geochemistry, Geophysics, Geosystems* 17, 4078–4091. https://doi.org/10.1002/2016GC006457

Burgisser, A., Scaillet, B. (2007) Redox evolution of a degassing magma rising to the surface. *Nature* 445, 194–197. https://doi.org/10.1038/nature05509

Burgisser, A., Alletti, M., Scaillet, B. (2015) Simulating the behavior of volatiles belonging to the C–O–H–S system in silicate melts under magmatic conditions with the software D-Compress. *Computers & Geosciences* 79, 1–14. https://doi.org/10.1016/j.cageo.2015.03.002

Candela, P.A. (1986) The evolution of aqueous vapor from silicate melts: Effect on oxygen fugacity. *Geochimica et Cosmochimica Acta* 50, 1205–1211. https://doi.org/10.1016/0016-7037(86)90403-5

Cottrell, E., Birner, S., Brounce, M., Davis, F., Waters, L., Kelley, K. (2021) Oxygen fugacity across tectonic settings. In: Moretti, R., Neuville, D.R. (Eds.) *Magma Redox Geochemistry*. American Geophysical Union, Hoboken, 33–61. https://doi.org/10.1002/9781119473206.ch3

Danyushevsky, L.V., Plechov, P. (2011) Petrolog3: Integrated software for modeling crystallization processes. *Geochemistry, Geophysics, Geosystems* 12, Q07021. https://doi.org/10.1029/2011GC003516

Ding, S., Plank, T., Wallace, P.J., Rasmussen, D.J. (2023) Sulfur_X: A Model of Sulfur Degassing During Magma Ascent. *Geochemistry, Geophysics, Geosystems* 24, e2022GC010552. https://doi.org/10.1029/2022GC010552

Fortin, M.-A., Riddle, J., Desjardins-Langlais, Y., Baker, D.R. (2015) The effect of water on the sulfur concentration at sulfide saturation (SCSS) in natural melts. *Geochimica et Cosmochimica Acta* 160, 100–116. https://doi.org/10.1016/j.gca.2015.03.022

Gaillard, F., Scaillet, B. (2009) The sulfur content of volcanic gases on Mars. *Earth and Planetary Science Letters* 279, 34–43. https://doi.org/10.1016/j.epsl.2008.12.028

Gaillard, F., Scaillet, B., Arndt, N.T. (2011) Atmospheric oxygenation caused by a change in volcanic degassing pressure. *Nature* 478, 229–232. https://doi.org/10.1038/nature10460

Havlicek, P., Hradecky, P., Hrubes, M., Kyel, P., Mlcoch, B. *et al*. (2000) Estudio Geológico Y Reconocimiento De La Amenaza Geológica En El Área De León - La Paz Centro Y Malpasillo, Praga-Managua 2000, Reporte Final (Servicio Geológico Checo, CGU, en cooperación con Instituto Nicaragüense de Estudios Territoriales, INETER).

Hazlett, R.W. (1977) *Geology and hazards of the San Cristóbal volcanic complex, Nicaragua*. PhD Thesis, Dartmouth College.

Hirata, Y., Ueta, K., Miyawaki, R., Iemura, K., Yokoyoma, T., Miyawaki, A. (2020) Tephra stratigraphy and an about 4000-year-old slope failure on Janoo volcano, NW Aso Caldera. *Transactions, Japanese Geomorphological Union* 41, 27–47. https://doi.org/10.60380/tjgu.41.1_27

Humphreys, M.C.S., Brooker, R.A., Fraser, D.G., Burgisser, A., Mangan, M.T., McCammon, C. (2015) Coupled Interactions between Volatile Activity and Fe Oxidation State during Arc Crustal Processes. *Journal of Petrology* 56, 795–814. https://doi.org/10.1093/petrology/egv017

Iacono-Marziano, G., Morizet, Y., Le Trong, E., Gaillard, F. (2012) New experimental data and semi-empirical parameterization of H_2O–CO_2 solubility in mafic melts. *Geochimica et Cosmochimica Acta* 97, 1–23. https://doi.org/10.1016/j.gca.2012.08.035

Kawaguchi, M., Hasenaka, T., Koga, K.T., Rose-Koga, E.F., Yasuda, A., Hokanishi, N., Mori, Y., Shimizu, K., Ushikubo, T. (2021) Persistent gas emission originating from a deep basaltic magma reservoir of an active volcano: the case of Aso volcano, Japan. *Contributions to Mineralogy and Petrology* 176, 6. https://doi.org/10.1007/s00410-020-01761-6

Kelley, K.A., Cottrell, E. (2012) The influence of magmatic differentiation on the oxidation state of Fe in a basaltic arc magma. *Earth and Planetary Science Letters* 329–330, 109–121. https://doi.org/10.1016/j.epsl.2012.02.010

Kress, V.C., Carmichael, I.S.E. (1991) The compressibility of silicate liquids containing Fe_2O_3 and the effect of composition, temperature, oxygen fugacity and pressure on their redox states. *Contributions to Mineralogy and Petrology* 108, 82–92. https://doi.org/10.1007/BF00307328

Métrich, N., Allard, P., Aiuppa, A., Bani, P., Bertagnini, A. *et al.* (2011) Magma and Volatile Supply to Post-collapse Volcanism and Block Resurgence in Siwi Caldera (Tanna Island, Vanuatu Arc). *Journal of Petrology* 52, 1077–1105. https://doi.org/10.1093/petrology/egr019

Miyabuchi, Y., Watanabe, K. (1997) Eruption Ages of Holocene Tephras from Aso Volcano, Southwestern Japan, Inferred from ^{14}C Ages of Buried Andisols. *Bulletin of the Volcanological Society of Japan* 42, 403–408. https://doi.org/10.18940/kazan.42.6_403

Miyabuchi, Y., Hanada, D., Niimi, H., Kobayashi, T. (2013) Stratigraphy, grain-size and component characteristics of the 2011 Shinmoedake eruption deposits, Kirishima Volcano, Japan. *Journal of Volcanology and Geothermal Research* 258, 31–46. https://doi.org/10.1016/j.jvolgeores.2013.03.027

Moussallam, Y., Rose-Koga, E.F., Koga, K.T., Médard, E., Bani, P., Devidal, J.-L., Tari, D. (2019) Fast ascent rate during the 2017–2018 Plinian eruption of Ambae (Aoba) volcano: a petrological investigation. *Contributions to Mineralogy and Petrology* 174, 90. https://doi.org/10.1007/s00410-019-1625-z

Moussallam, Y., Médard, E., Georgeais, G., Rose-Koga, E.F., Koga, K.T. *et al.* (2021) How to turn off a lava lake? A petrological investigation of the 2018 intra-caldera and submarine eruptions of Ambrym volcano. *Bulletin of Volcanology* 83, 36. https://doi.org/10.1007/s00445-021-01455-2

Moussallam, Y., Lee, H.J., Ding, S., DeLessio, M., Everard, J.L. *et al.* (2023) Temperature of the Villarrica Lava Lake from 1963 to 2015 Constrained by Phase-Equilibrium and a New Glass Geothermometer for Basaltic Andesites. *Journal of Petrology* 64, egad003. https://doi.org/10.1093/petrology/egad003

Muth, M.J., Wallace, P.J. (2021) Slab-derived sulfate generates oxidized basaltic magmas in the southern Cascade arc (California, USA). *Geology* 49, 1177–1181. https://doi.org/10.1130/G48759.1

Nairn, I., Scott, B., Giggenbach, W. (1988) Yasur volcanic investigations, Vanuatu September 1988. *New Zealand Geological Survey Report G* 134.

Peccia, A., Moussallam, Y., Plank, T., DallaSanta, K., Polvani, L., Burgisser, A., Larsen, J., Schaefer, J. (2023) A New Multi-Method Assessment of Stratospheric Sulfur Load From the Okmok II Caldera-Forming Eruption of 43 BCE. *Geophysical Research Letters* 50, e2023GL103334. https://doi.org/10.1029/2023GL103334

Pistolesi, M., Aravena, A., Costantini, L., Vigiani, C., Cioni, R., Bonadonna, C. (2021) Explosive Behavior of Intermediate Magmas: The Example of Cotopaxi Volcano (Ecuador). *Geochemistry, Geophysics, Geosystems* 22, e2021GC009991. https://doi.org/10.1029/2021GC009991

Robidoux, P., Aiuppa, A., Rotolo, S.G., Rizzo, A.L., Hauri, E.H., Frezzotti, M.L. (2017) Volatile contents of mafic-to-intermediate magmas at San Cristóbal volcano in Nicaragua. *Lithos* 272–273, 147–163. https://doi.org/10.1016/j.lithos.2016.12.002

Shi, S., Barth, A., Plank, T., Towbin, W., Flores, O., Arias, C. (2021) Magma stalling weakens eruption. *AGU Fall Meeting*, New Orleans, LA, 13–17 December 2021, V25E-09 (abstract).

Shi, S., Towbin, W.H., Plank, T., Barth, A., Rasmussen, D., Moussallam, Y., Lee, H.J., Menke, W. (2024) PyIRoGlass: An open-source, Bayesian MCMC algorithm for fitting baselines to FTIR spectra of basaltic-andesitic glasses. *Volcanica* 7, 471–501. https://doi.org/10.30909/vol.07.02.471501

Suzuki, Y., Yasuda, A., Hokanishi, N., Kaneko, T., Nakada, S., Fujii, T. (2013) Syneruptive deep magma transfer and shallow magma remobilization during the 2011 eruption of Shinmoe-dake, Japan—Constraints from melt inclusions and phase equilibria experiments. *Journal of Volcanology and Geothermal Research* 257, 184–204. https://doi.org/10.1016/j.jvolgeores.2013.03.017

Taracsák, Z., Mather, T.A., Ding, S., Plank, T., Brounce, M., Pyle, D.M., Aiuppa, A., EIMF (2023) Sulfur from the subducted slab dominates the sulfur budget of the mantle wedge under volcanic arcs. *Earth and Planetary Science Letters* 602, 117948. https://doi.org/10.1016/j.epsl.2022.117948

Zhang, H.L., Cottrell, E., Solheid, P.A., Kelley, K.A., Hirschmann, M.M. (2018) Determination of $Fe^{3+}/\Sigma Fe$ of XANES basaltic glass standards by Mössbauer spectroscopy and its application to the oxidation state of iron in MORB. *Chemical Geology* 479, 166–175. https://doi.org/10.1016/j.chemgeo.2018.01.006